

New synthesis models of consistent extragalactic background light over cosmic time

Vikram Khaire^{1,2*} and Raghunathan Srianand³

¹*Department of Physics, University of California, Santa Barbara, CA 93106-9530, USA*

²*National Centre for Radio Astrophysics, Tata Institute of Fundamental Research, Pune 411007, India*

³*Inter-University Centre for Astronomy and Astrophysics, Post Bag 4, Pune 411007, India*

ABSTRACT

We present new synthesis models of the extragalactic background light (EBL) from far infra-red (FIR) to TeV γ -rays, with an emphasis on the extreme ultraviolet (UV) background which is responsible for the observed ionization and thermal state of the intergalactic medium across the cosmic time. Our models use updated values of the star formation rate density and dust attenuation in galaxies, QSO emissivity, and the distribution of H I gas in the IGM. Two of the most uncertain parameters in these models, the escape fraction of H I ionizing photons from galaxies and the spectral energy distribution (SED) of QSOs, are determined to be consistent with the latest measurements of H I and He II photoionization rates, the He II Lyman- α effective optical depths, various constraints on H I and He II reionization history and many measurements of the local EBL from soft X-rays till γ -rays. We calculate the EBL from FIR to TeV γ -rays by using FIR emissivities from our previous work and constructing an average SED of high-energy emitting QSOs, i.e., type-2 QSOs and blazars. For public use, we also provide the EBL models obtained using different QSO SEDs at extreme-UV energies over a wide range of redshifts. These can be used to quantify uncertainties in the parameters derived from photoionization models and numerical simulations originating from the allowed variations in the UV background radiation.

Key words: Cosmology: diffuse radiation – galaxies: evolution – quasars: general – galaxies: intergalactic medium

1 INTRODUCTION

The radiation background set-up by light emitted from all galaxies and Quasi-Stellar Objects (QSOs) throughout the cosmic time is known as extragalactic background light (EBL). The full spectrum of EBL carries imprints of cosmic structure formation, therefore, it serves as an important tool to study formation and evolution of galaxies. It is also essential for studying the propagation of high energy γ -rays from distant sources since the EBL can annihilate γ -rays upon collision (Gould & Schréder 1966; Stecker et al. 1992; Ackermann et al. 2012). The EBL is playing a key role in rapidly developing γ -ray astronomy to address fundamental questions related to the production of γ -rays, their acceleration mechanism (Stecker et al. 2007) and cosmic magnetic fields in the intergalactic space (Neronov & Vovk 2010; Tavecchio et al. 2011; Arlen et al. 2012; Finke et al. 2015).

A small part of this EBL at extreme-UV energies ($E >$

13.6 eV or $\lambda < 912 \text{ \AA}$) is known as the UV background (UVB). The UVB is responsible for maintaining the observed ionization and thermal state of the diffuse intergalactic medium (IGM; see reviews by Meiksin 2009; McQuinn 2016), a reservoir that is believed to contain more than 90% of total baryons in the Universe.

The sources that setup UVB also drive the major phase transitions of the IGM, the H I and He II reionization. Starting from the time when first galaxies were born, the process of H I reionization is believed to be completed around $z \sim 6$ as suggested by various observations of H I Lyman- α forest in the spectra of high redshift QSOs (e.g., Becker et al. 2001; Fan et al. 2006; Goto et al. 2011; McGreer et al. 2015; Greig et al. 2017; Bañados et al. 2017), electron scattering optical depth to the cosmic microwave background (CMB Larson et al. 2011; Planck Collaboration et al. 2016a) and decreasing fraction of Lyman- α emitting galaxies at high redshifts (e.g., Schenker et al. 2014; Choudhury et al. 2015; Mesinger et al. 2015; Mason et al. 2017). The He II reionization is believed to be started by hard He II ionizing radi-

* E-mail:vkhaire@physics.ucsb.edu

ation emitted by QSOs and took longer time to complete. It was completed around $z \sim 2.8$ as suggested by observations of He II Lyman- α forest in handful of QSOs (e.g., Kriss et al. 2001; Shull et al. 2004, 2010; Fechner et al. 2006; Worseck et al. 2011, 2016) and measurements of a peak in the redshift evolution of IGM temperature (Lidz et al. 2010; Becker et al. 2011; Hiss et al. 2017). During these reionization events, spectrum of the UVB decides the extra energy gained by photoelectrons, which gets redistributed in the IGM driving its thermal state (Hui & Gnedin 1997). Subsequently the thermal history of the IGM is driven by the UVB and adiabatic expansion of the Universe.

Thermal history of the IGM has its imprint on the small scale structures in the IGM through pressure smoothing that can be probed by correlation analysis of closely spaced QSO sightlines (e.g., Gnedin & Hui 1998; Schaye 2001; Kulkarni et al. 2015; Rorai et al. 2017). Photoheating by the UVB can also provide negative feedback that can suppress the star formation in dwarf galaxies (Efstathiou 1992; Weinberg et al. 1997) and decide the faint end shapes of the high- z luminosity functions (e.g., Samui et al. 2007). Therefore the UVB is one of the most important inputs in the cosmological simulations of structure formation and the IGM (e.g., Hernquist et al. 1996; Davé et al. 1999; Springel et al. 2001).

Perhaps the most important and frequent application of UVB is to study the metal absorption lines ubiquitously observed in QSO absorption spectra. It is because the EBL from extreme-UV to soft X-ray not only ionizes hydrogen and helium but also several metals such as Mg, C, Si, N, O, Ne. Therefore, the UVB serves as an essential ingredient to study the physical and chemical properties of the gas observed in the QSO absorption spectra originating either from low-density gas in the IGM or high-density gas in the vicinity of intervening galaxies known as a circumgalactic medium (CGM). In the studies of metal absorption lines, the UVB is crucial for relating observed ionic abundances to metal abundances, in order to determine the metal production and their transport to CGM by galaxies (e.g., Ferrara et al. 2005; Lehner et al. 2014; Peebles et al. 2014) and the time evolution of the cosmic metal density (e.g., Songaila & Cowie 1996; Bergeron et al. 2002; Schaye et al. 2003; Aracil et al. 2004; D’Odorico et al. 2013; Shull et al. 2014; Prochaska et al. 2017; Muzahid et al. 2017). At low redshifts, the UVB is essential for studying the ionization mechanism of highly ionized species such as O VI (e.g., Danforth & Shull 2005; Tripp et al. 2008; Muzahid et al. 2012; Savage et al. 2014; Pachat et al. 2016; Narayanan et al. 2018) and Ne VIII (e.g., Savage et al. 2005, 2011; Narayanan et al. 2012; Meiring et al. 2013; Hussain et al. 2015, 2017; Pachat et al. 2017) to understand their contribution to the warm-hot IGM and missing baryons (see Shull et al. 2012).

The local EBL ($z = 0$) at most wavelength ranges can be observed directly (e.g., Dwek & Arendt 1998; Dole et al. 2006; Ajello et al. 2008), however there are no such direct observations of the UVB because the interstellar-medium of our Milky-way attenuates it completely. Therefore, one needs to model the UVB spectrum and its redshift evolution. There are, however, integral constraints on the UVB obtained from the measurements of H I and He II photoionization rates. The

H I photoionization rates (Γ_{HI}) can be measured by using the observations of 21 cm truncation and H α fluorescence in nearby galaxies (e.g., Sunyaev 1969; Dove & Shull 1994; Adams et al. 2011; Fumagalli et al. 2017), by analyzing the incidence of Lyman- α forest lines in the proximity of QSOs (e.g., Bajtlik et al. 1988; Kulkarni & Fall 1993; Srianand & Khare 1996; Dall’Aglio et al. 2008), and by reproducing various statistical properties of the observed Lyman- α forest in the cosmological simulations of the IGM where Γ_{HI} is treated as one of the free parameters (e.g., Rauch et al. 1997; Bolton & Haehnelt 2007; Becker & Bolton 2013; Kollmeier et al. 2014; Shull et al. 2015; Gaikwad et al. 2017a,b, 2018). One can also infer the He II photoionization rate (Γ_{HeII}) using the measurements of Γ_{HI} and the observed H I column density distribution as demonstrated in Khaire (2017). These measurements play crucial role in calibrating the synthesis models of UVB at different redshifts.

The full synthesis model of UVB was pioneered by Haardt & Madau (1996) (see also Fardal et al. 1998) using cosmological radiative transfer calculations following the footsteps of previous work (Miralda-Escude & Ostriker 1990; Shapiro et al. 1994; Giroux & Shapiro 1996). Over the last two decades, there are some variations of their UVB models (Haardt & Madau 2001, 2012) and the UVB models by other groups (Shull et al. 1999; Faucher-Giguère et al. 2009). Out of these, most recent models¹ are Faucher-Giguère et al. (2009, hereafter FG09) and Haardt & Madau (2012, hereafter HM12). These recent models are not completely consistent with the new observations such as the Γ_{HI} at $z < 0.5$ (Shull et al. 2015; Gaikwad et al. 2017a,b; Viel et al. 2017; Gurvich et al. 2017) and $z > 3$ (Becker & Bolton 2013). These models also use old values of many observables relevant to UVB which are significantly different from current measurements, such as, the type-1 QSO emissivity (Khaire & Srianand 2015a, hereafter KS15a), galaxy emissivity (Behroozi et al. 2013; Madau & Dickinson 2014; Khaire & Srianand 2015b, hereafter KS15b) and various constraints on H I and He II reionization (Choudhury et al. 2015; Planck Collaboration et al. 2016b; Greig & Mesinger 2017; Worseck et al. 2016). In light of all these issues, and the fact that there are only few independent UVB models available in the literature, we present new synthesis models of EBL focusing on the UVB and extending it till TeV γ -rays from far infra-red (FIR).

In our EBL models we use the updated type-1 QSO emissivity obtained from a compilation of recent QSO luminosity functions KS15a. Our models use galaxy emissivity till FIR wavelengths obtained from the updated star formation and dust attenuation history of the Universe from KS15b. These are determined through a large compilation of multi-wavelength galaxy luminosity functions (see KS15b, and references therein). We also use updated H I distribution of the IGM from Inoue et al. (2014) that is obtained from a large number of different observations (mentioned in Section 2). Apart from these, there are two additional important input parameters required to model the UVB; the

¹ Excluding a QSO only model by Madau & Haardt (2015) and a recent Puchwein et al. (2018) model which appeared while we were finalizing the paper.

average escape fraction of H I ionizing photons from galaxies (f_{esc}) and the mean spectral energy distribution (SED) of type-1 QSOs at extreme-UV wavelengths. However, the observational constraints on these are either not available or poor.

The measurement of f_{esc} from individual galaxies as well as large surveys has been proven to be a challenging endeavor (Vanzella et al. 2010; Siana et al. 2015; Mostardi et al. 2015). There are handful of galaxies at $z < 0.5$ which show emission of H I ionizing photons with f_{esc} ranging from 2 to 46% (Bergvall et al. 2006; Leitet et al. 2013; Borthakur et al. 2014; Leitherer et al. 2016; Izotov et al. 2016b,a, 2018) and only two galaxies at $z > 3$ with large f_{esc} of the order of 50% (Vanzella et al. 2016; de Barros et al. 2016; Shapley et al. 2016). However, all of these are few exceptional cases, as most studies with large number of galaxies provide only upper limits on the average f_{esc} (e.g., Cowie et al. 2009; Bridge et al. 2010; Siana et al. 2010; Guaita et al. 2016; Matthee et al. 2017; Grazian et al. 2017; Japelj et al. 2017; Smith et al. 2016, see left-hand panel of Fig. 3 and Table A1 for summary of recent measurements). On the other hand, there are measurements of QSO SED at extreme-UV from large number of QSOs probing rest-wavelength $\lambda < 912 \text{ \AA}$ (e.g., Zheng et al. 1997; Telfer et al. 2002; Scott et al. 2004; Shull et al. 2012; Stevans et al. 2014; Lusso et al. 2015; Tilton et al. 2016). However, under the assumption that QSO SED follows a power-law, $f_{\nu} \propto \nu^{\alpha}$ at $\lambda < 912 \text{ \AA}$, the values of power-law index α obtained from these measurements show large variation (-0.56 to -1.96; see table 1 of Khaire 2017, for the summary of these measurements). Also, the smallest wavelength probed in these studies is $\sim 425 \text{ \AA}$ whereas the UVB model calculations extrapolate it upto soft X-rays ($\lambda \lesssim 20 \text{ \AA}$).

Because of these uncertainties, we choose to determine the $f_{\text{esc}}(z)$ and α which are required to consistently reproduce various observational constraints on the UVB following Khaire et al. (2016) and Khaire (2017). We obtain the $f_{\text{esc}}(z)$ to reproduce the Γ_{HI} measurements and various constraints on H I reionization. In our fiducial UVB model, we use $\alpha = -1.8$ which was found to reproduce the measured He II Lyman- α effective optical depths as a function of z and the epoch of He II reionization (see Khaire 2017). However, we also provide UVB models for α varying from -1.4 to -2.0 in the interval of 0.1. Moreover, following Sazonov et al. (2004) we modify the SED of type-1 QSOs to include the type-2 QSOs and blazars in order to calculate the X-ray and γ -ray part of the EBL consistent with various measurements of the local X-ray and γ -ray backgrounds. Our full EBL spans more than fifteen orders of magnitude in wavelength from FIR to TeV γ -rays.

The paper is organized as follows. In Section 2, we briefly discuss the basic cosmological radiative transport theory used for calculating the EBL. In Section 3, we explain the emissivities used in our EBL. We discuss the QSO emissivity, their SEDs, the galaxy emissivity, $f_{\text{esc}}(z)$ and the diffuse emissivity from the IGM. In Section 4, we discuss our fiducial model and its predictions for H I and He II photoionization rates, reionization histories, full spectrum of the EBL from FIR to γ -rays and the detailed uncertainties in the UVB models. In Section 5, we summarize our main results. In Appendix we show plots for various UVB models generated for different α , provide relevant tables of photoioniza-

tion and photoheating rates and optical depths encountered by γ -ray photons due to the EBL. Throughout the paper, we have used the cosmological parameters $\Omega_m = 0.3$, $\Omega_{\Lambda} = 0.7$ and $H_0 = 70 \text{ km s}^{-1} \text{ Mpc}^{-1}$ consistent with measurements from Planck Collaboration et al. (2016a). All our EBL tables in machine-readable format are publicly available to download at IUCAA-ftp and a webpage.

2 COSMOLOGICAL RADIATIVE TRANSFER

The specific intensity, J_{ν_0} , of the EBL (in units of $\text{erg cm}^{-2} \text{ s}^{-1} \text{ Hz}^{-1} \text{ sr}^{-1}$) at frequency ν_0 and redshift z_0 is obtained using the following integral (Peebles 1993; Haardt & Madau 1996):

$$J_{\nu_0}(z_0) = \frac{c}{4\pi} \int_{z_0}^{\infty} dz \frac{(1+z_0)^3 \epsilon_{\nu}(z)}{(1+z) H(z)} e^{-\tau_{\text{eff}}(\nu_0, z_0, z)}. \quad (1)$$

Here, c is speed of light, $H(z) = H_0 \sqrt{\Omega_m(1+z)^3 + \Omega_{\Lambda}}$ is the Hubble parameter, $\epsilon_{\nu}(z)$ is a volume averaged comoving specific emissivity at frequency ν with $\nu = \nu_0(1+z)/(1+z_0)$ and $\tau_{\text{eff}}(\nu_0, z_0, z)$ is an effective optical depth encountered by photons arriving at redshift z_0 having frequency ν_0 which were emitted at redshift $z \geq z_0$ with frequency ν . The τ_{eff} from the IGM is negligibly small for EBL at optical and higher wavelengths. However, it can be significantly larger for extreme-UV radiation due to atomic gas in the IGM. Therefore, it needs to be accurately calculated using detailed radiative transfer through hydrogen and helium gas of the IGM present in the form of discrete absorbers.

The effective optical depth is defined as $\tau_{\text{eff}} = -\ln(< e^{-\tau} >)$ where τ is continuum optical depth through absorbers and $< e^{-\tau} >$ is an average transmission over all line of sights. Assuming that the discrete absorbers along any line of sight are Poisson distributed, the τ_{eff} is obtained by (see Paresce et al. 1980; Padmanabhan 2002),

$$\tau_{\text{eff}}(\nu_0, z_0, z) = \int_{z_0}^z dz' \int_0^{\infty} dN_{\text{HI}} \frac{\partial^2 N}{\partial N_{\text{HI}} \partial z'} (1 - e^{-\tau_{\nu'}}). \quad (2)$$

Here, $\partial^2 N / \partial N_{\text{HI}} \partial z' = f(N_{\text{HI}}, z')$ is a bivariate distribution of the absorbers with respect to their redshift z' and H I column density N_{HI} , also known as a column density distribution function of H I. The $\tau_{\nu'}$ in equation (2) is a continuum optical depth encountered by photons arriving at redshift z_0 with frequency ν_0 which were emitted at redshift $z' \geq z_0$ with frequency $\nu' = \nu_0(1+z')/(1+z_0)$. The $\tau_{\nu'}$, by ignoring a negligible contribution from metals and dust in the IGM, is given by

$$\tau_{\nu'} = N_{\text{HI}} \sigma_{\text{HI}}(\nu') + N_{\text{HeI}} \sigma_{\text{HeI}}(\nu') + N_{\text{HeII}} \sigma_{\text{HeII}}(\nu'), \quad (3)$$

where N_x and σ_x are the column densities and photoionization cross-sections of species x . Unlike for H I, the column density distribution of He II and He I are not available from direct observations.

There are very few line of sights where N_{HeII} has been measured (e.g., Zheng et al. 2004; Muzahid et al. 2011; McQuinn & Worseck 2014). Therefore, the amount of N_{HeI} and N_{HeII} in the H I absorbers needs to be inferred through photoionization modeling. For that we rewrite the equation (3) as,

$$\tau_{\nu'} = N_{\text{HI}} \left[\sigma_{\text{HI}}(\nu') + \zeta \sigma_{\text{HeI}}(\nu') + \eta \sigma_{\text{HeII}}(\nu') \right], \quad (4)$$

where $\zeta = N_{\text{HeI}}/N_{\text{HI}}$ and $\eta = N_{\text{HeII}}/N_{\text{HI}}$. Under the assumption that the IGM absorbers are in photoionization equilibrium with the UVB, η is obtained by solving following quadratic equation (Fardal et al. 1998; Faucher-Giguère et al. 2009; Haardt & Madau 2012)

$$\frac{n_{\text{He}}}{4n_{\text{H}}} \frac{\Gamma_{\text{HI}}}{n_e \alpha_{\text{HI}}(\text{T})} \frac{\sigma_{912} N_{\text{HI}}}{(1 + A \sigma_{912} N_{\text{HI}})} = \sigma_{228} N_{\text{HeII}} \\ + \frac{\Gamma_{\text{HeII}}}{n_e \alpha_{\text{HeII}}(\text{T})} \frac{\sigma_{\text{HeII}} N_{\text{HeII}}}{(1 + B \sigma_{228} N_{\text{HeII}})}. \quad (5)$$

Here, n_e is the electron density, σ_{228} and σ_{912} are the photoionization cross-sections of He II and H I at 228 Å and 912 Å, respectively, the constants A and B are obtained to fit the numerical results and Γ_x is the photoionization rate for species x . The Γ_x at any redshift z_0 is defined as

$$\Gamma_x(z_0) = \int_{\nu_x}^{\infty} d\nu \frac{4\pi J_{\nu}(z_0)}{h\nu} \sigma_x(\nu), \quad (6)$$

where, ν_x is a threshold frequency for ionization of species x . The ionization threshold energies $h\nu_x$, where h is the Planck's constant, for H I, He I and He II are 13.6, 24.4 and 54.4 eV, respectively. Following Haardt & Madau (2012) we take $A = 0.02$ and $B = 0.25$, the relation between n_e and N_{HI} as $n_e = 1.024 \times 10^{-6} (N_{\text{HI}} \Gamma_{\text{HI}})^{(2/3)} \text{cm}^{-3}$ and $\text{T} = 20000$ K. We use $\zeta = \eta n_e \alpha_{\text{HeI}}(\text{T})/\Gamma_{\text{HeI}}$. We verified these parameters by modeling the IGM clouds as plane parallel slabs with the line-of-sight thickness equal to the Jeans length (Schaye 2001) using CLOUDY13 software (Ferland et al. 2013).

We take $f(N_{\text{HI}}, z)$ from Inoue et al. (2014) at all z . It has been obtained by fitting various observations over $z = 0 - 6$ such as the number distribution and column density distribution of optically thin H I Lyman- α absorbers (Weymann et al. 1998; Kim et al. 2001; Janknecht et al. 2006; Kim et al. 2013), optically thick Lyman limit absorbers (Péroux et al. 2005; Rao et al. 2006; Songaila & Cowie 2010; Prochaska et al. 2010; O'Meara et al. 2013; Fumagalli et al. 2013) and damped Lyman- α absorbers (O'Meara et al. 2007; Noterdaeme et al. 2009, 2012; Prochaska et al. 2014), the mean transmission and optical depth of the IGM to Lyman- α photons (Faucher-Giguère et al. 2008; Kirkman et al. 2007; Fan et al. 2006; Becker et al. 2013) and the mean free path of H I ionizing photons through IGM (Prochaska et al. 2009; Worseck et al. 2014). The $f(N_{\text{HI}}, z)$ calculated at $z = 5.5$ and 6 from high-resolution hydrodynamic simulations for the measured Γ_{HI} values match reasonably well with the $f(N_{\text{HI}}, z)$ from Inoue et al. (2014), as shown in Khaire et al. (2016). This consistency motivates us to use this $f(N_{\text{HI}}, z)$ even at $z > 6$ where direct observations are not possible because of strong Gunn-Peterson effect (Gunn & Peterson 1965). See Section 4.4.3, for uncertainties in the UVB arising when different $f(N_{\text{HI}}, z)$ is used in our calculations.

3 EMISSIVITY

The comoving source emissivity ϵ_{ν} is the most important quantity in the EBL calculations. The ϵ_{ν} is contributed by photons emitted from three different sources; the QSOs (ϵ_{ν}^Q) by accretion of matter onto supermassive blackholes, the galaxies (ϵ_{ν}^G) from the radiation emitted by their stellar population and re-processed by dust in their interstellar

medium, and the re-processed diffuse emission from the photoionized IGM (ϵ_{ν}^d). Therefore,

$$\epsilon_{\nu}(z) = \epsilon_{\nu}^Q(z) + \epsilon_{\nu}^G(z) + \epsilon_{\nu}^d(z). \quad (7)$$

In the following subsections, we discuss the emissivity from these different sources used in our EBL calculations. Note that, we do not consider non-standard sources such as dark-matter annihilation which has been shown to have negligible contribution to the EBL (e.g., Zavala et al. 2011; Ajello et al. 2015; Gaikwad et al. 2017a, KS15a).

3.1 QSO Emissivity

The QSO emissivity $\epsilon_{\nu_0}^Q(z)$ is obtained by integrating the QSO luminosity function (QLF), $\phi(L_{\nu_0}, z)$, observed at frequency ν_0 and redshift z by

$$\epsilon_{\nu_0}^Q(z) = \int_{L_{\nu_0}^{\min}}^{\infty} L_{\nu_0}(z) \phi(L_{\nu}, z) dL_{\nu_0}, \quad (8)$$

where $L_{\nu_0}^{\min}$ is the minimum luminosity of QSOs at ν_0 used in the integration. This $\epsilon_{\nu_0}^Q(z)$ can be used to obtain the QSO emissivity $\epsilon_{\nu}^Q(z)$ at any frequency ν by using the mean SED of QSOs (k_{ν}) as

$$\epsilon_{\nu}^Q(z) = k_{\nu} * \epsilon_{\nu_0}^Q(z). \quad (9)$$

We use $\epsilon_{\nu_0}^Q(z) = \epsilon_{1000}^Q(z)$ obtained at $\nu_0 = c/1000$ Å (or $h\nu_0 = 12.4$ eV) from KS15a. In KS15a, the $\epsilon_{\nu_0}^Q(z)$ values were obtained by using a compilation of recent QLFs (of type-1 QSOs) at different wavebands (Schulze et al. 2009; Croom et al. 2009; Glikman et al. 2011; Masters et al. 2012; Ross et al. 2013; Palanque-Delabrouille et al. 2013; McGreer et al. 2013; Kashikawa et al. 2015). For each QLF, $\epsilon_{\nu_0}^Q$ was obtained at the observed frequency $\nu_0 < c/1000$ Å, by using equation (8) with $L_{\nu}^{\min} = 0.01 L_{\nu_0}^*$, where $L_{\nu_0}^*$ is the characteristic luminosity of that QLF. Then these $\epsilon_{\nu_0}^Q$ values (see Table 1 of KS15a) were converted at frequency $c/1000$ Å using a form of QSO SED applicable at $\lambda \geq 1000$ Å. A simple fit through the redshift evolution of $\epsilon_{1000}^Q(z)$ in units of $\text{erg s}^{-1} \text{Hz}^{-1} \text{Mpc}^{-3}$ is given by²,

$$\epsilon_{1000}^Q(z) = 4.53 \times 10^{24} (1+z)^{5.9} \frac{\exp(-0.36z)}{\exp(2.2z) + 25.1}. \quad (10)$$

In the left-hand panel of Fig. 1, we show this fit with the individual $\epsilon_{1000}^Q(z)$ values for each QLF compiled in KS15a. For comparison, we also show the $\epsilon_{1000}^Q(z)$ used by HM12 which was obtained using the QLFs compiled by Hopkins et al. (2007). At $z < 3$ the $\epsilon_{1000}^Q(z)$ by KS15a is higher than HM12 because the recent QLFs (e.g., Croom et al. 2009; Palanque-Delabrouille et al. 2013) have higher $L_{\nu_0}^*$ and characteristic number density $\Phi_{\nu_0}^*$. This higher QSO emissivity was crucial in resolving the photon underproduction crisis claimed by Kollmeier et al. (2014). We are using the same SED at $\lambda > 1000$ Å as used in KS15a, however, at $\lambda < 1000$ Å we use a modified form of the SED.

The QSO emissivity mentioned in equation (10) is contributed by type-1 QSOs alone. Note that to calculate the background radiation in extreme-UV, one does not need to consider the contribution from type-2 QSOs. According

² The $\epsilon_{1000}^Q(z)$ is obtained by multiplying $(1000/912)^{1.4}$ to the $\epsilon_{912}^Q(z)$ provided in KS15a

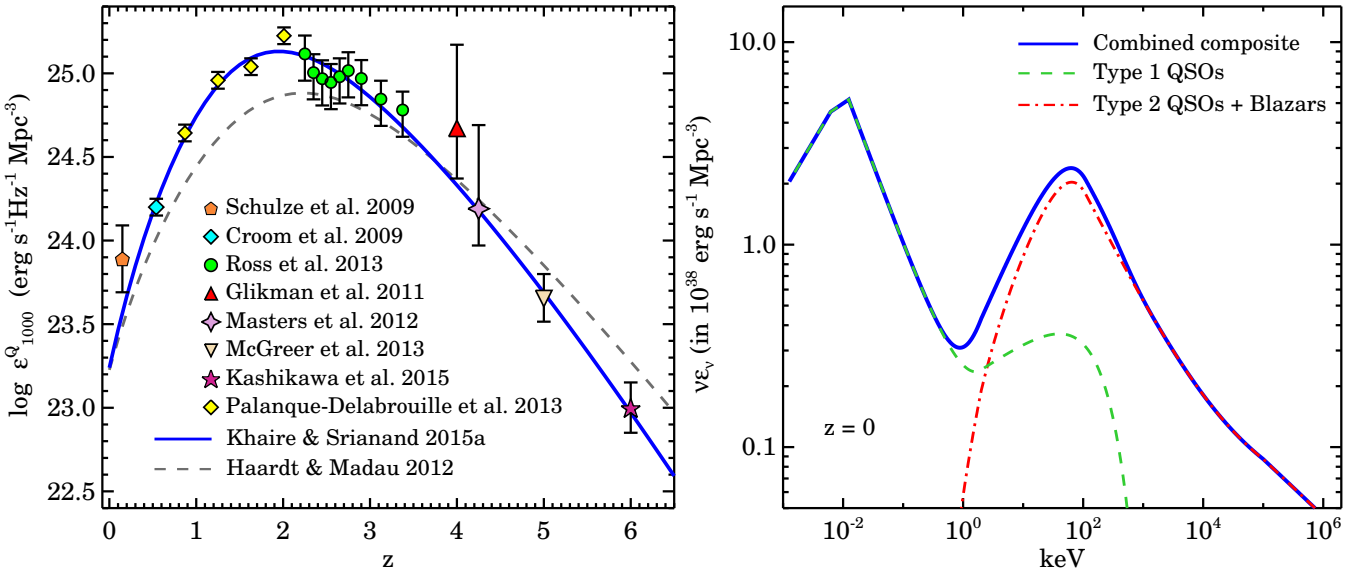


Figure 1. Left-hand panel: the specific QSO emissivity at 1000 Å ($\epsilon_{\nu_{1000}}^Q$) with z . Data points are taken from the compilation of recent QSO luminosity functions by Khaire & Srianand (2015a, see their table 1). Blue solid curve is a simple fit through the $\epsilon_{\nu_{1000}}^Q$ values (equation 10). Dashed curve is the $\epsilon_{\nu_{1000}}^Q$ used by HM12 which is obtained using the compilation of QSO luminosity functions by Hopkins et al. (2007). Right-hand panel: $z = 0$ QSO emissivity (solid curve) at different energies to illustrate our fiducial composite QSO SED (with $\alpha = -1.8$; equation 11). Dashed curve and dot-dash curve shows the adopted SED of Type-1 QSOs and high-energy emitting AGN template SED (i.e. Type-2 QSOs and blazars), respectively, normalized to get $\epsilon_{\nu_{1000}}^Q$ at $z = 0$.

to the standard unification scheme of active galactic nuclei (AGN; Antonucci 1993; Urry & Padovani 1995), different classes of QSOs arise due to differences in the orientation of QSOs along the direction of obscuring torus around their central engine with respect to us. Therefore, under the assumption of isotropic distribution of randomly oriented QSOs, to calculate the extreme-UV emissivities it is equivalent to assume that the extreme-UV photons are emitted either isotropically by type-1 QSOs alone or only along certain directions by both type-1 and type-2 QSOs. However, in the latter assumption one needs to correctly account for the fraction of type-2 QSOs. For simplicity, to calculate the UVB we choose the former assumption. However, to extend our EBL calculation to high energy X-rays, which are emitted isotropically by all types of QSOs, we need to incorporate contribution from type-2 QSOs.

This contribution in X-rays can be accounted self-consistently by using type-2 QSO luminosity function in soft and hard X-ray band and then modeling the distribution of different hydrogen column densities in obscuring torus, using intrinsic template of X-ray SEDs of QSOs and by fixing a contribution of extremely obscured Compton thick QSOs by comparing with measurements of the unresolved X-ray background (see for e.g., Comastri et al. 1995; Treister & Urry 2005; Gilli et al. 2007; Treister et al. 2009; Ballantyne et al. 2011). Similarly the contribution to γ -ray background from blazars can be modeled by generating the blazar luminosity function and their SED from luminosity functions of radio QSOs (e.g., Draper & Ballantyne 2009).

However, these X-ray population synthesis models require different fractions of Compton thick QSOs to generate the observed peak at ~ 30 keV in X-ray background and varying degree of obscuring hydrogen column densities

but still may not entirely reproduce the observed soft X-ray background (see, Cappelluti et al. 2017). Although this might be the most appropriate approach, given the large uncertainties involved in it we take a more simplistic approach which can provide an observationally consistent model of the EBL in X-ray energies useful for constructing ionization models for highly ionized metal species such as O VI, O VII, Ne VIII, Ne IX, Mg X. In particular, we follow the approach of Sazonov et al. (2004) and construct a template SED of type-1 and type-2 QSOs at X-ray energies. Our type-2 QSO SED not only accounts for the contribution of Compton thick AGNs but also includes γ -rays that will mostly come from beamed sources like blazars. This SED can be thought as a template SED for high-energy emitting AGNs. These SEDs are constructed such that when used in the EBL calculations they can reproduce a complete spectrum of observed X-ray and γ -ray background. The final QSO SED constructed in this way is given below.

Our final composite QSO SED (k_{ν}) is a combination of the SEDs from type-1 (k_{ν}^{Q1}) and type-2 QSOs including blazars (k_{ν}^{Q2}). Therefore,

$$k_{\nu} = k_{\nu}^{Q1} + k_{\nu}^{Q2} \quad (11)$$

We use a following SED for the type-1 QSOs:

$$k_{\nu}^{Q1} = \begin{cases} A_1 \left(\frac{h\nu}{6.2 \text{ eV}} \right)^{-0.5}, & h\nu < 6.2 \text{ eV} \\ A_2 \left(\frac{h\nu}{12.4 \text{ eV}} \right)^{-0.8}, & 6.2 < h\nu < 12.4 \text{ eV} \\ A_3 \left(\frac{h\nu}{12.4 \text{ eV}} \right)^{\alpha} \exp \left(\frac{\nu}{\nu_a} \right), & 12.4 \text{ eV} < h\nu < h\nu_a \\ A_4 \left(\frac{\nu}{\nu_a} \right)^{-0.8} \exp \left(\frac{-h\nu}{2 \text{ MeV}} \right), & h\nu > h\nu_a \end{cases} \quad (12)$$

where the normalizations are

$$A_1 = 2^{0.8}, \quad A_2 = 1, \quad A_3 = \exp\left(\frac{-12.4 \text{ eV}}{h\nu_a}\right),$$

$$A_4 = A_3 \exp\left(1 + \frac{h\nu_a}{2 \text{ MeV}}\right) \left(\frac{h\nu_a}{12.4 \text{ eV}}\right)^\alpha.$$

The power-law SED form and the indices at $h\nu < 12.4$ eV ($\lambda > 1000 \text{ \AA}$) are taken from the measurements of [Stevans et al. \(2014\)](#). At ionizing energies, $h\nu > 12.4 \text{ eV}$, we consider a range in power-law index α for our UVB models since there is no consensus on the observed value of α , as mentioned in Section 1. This power-law SED has been multiplied by $\exp(\nu/\nu_a)$ to get the excess in soft X-rays and the hard X-ray bump. However, the value of ν_a depends on the assumed value of α . Therefore for each α we have used a different $h\nu_a$ as given in Table 1. We calculated EBL by varying α in the interval of 0.1 from -1.4 , consistent with low- z ($z < 1.5$) measurements of [Stevans et al. \(2014\)](#), to $\alpha = -2$, consistent with high- z ($z \sim 2.5$) measurements of [Lusso et al. \(2015\)](#) and from radio-loud QSO sample of [Telfer et al. \(2002\)](#). For our fiducial UVB model, we use $\alpha = -1.8$ that has been shown to be consistent with the He II Lyman- α effective optical depth measurements ([Khaire 2017](#)). In the right-hand panel of Fig. 1, we show the type-1 QSO SED for $\alpha = -1.8$ normalized at ϵ_{1000}^Q at $z = 0$.

For type-2 QSOs and γ -ray emitting blazars, we adopt the following SED,

$$k_\nu^{Q2} = \begin{cases} B_1 p_\nu & h\nu < E_0 \\ B_2 p_\nu \left(\frac{h\nu}{E_0}\right)^{-0.24} \exp\left(\frac{-h\nu}{83 \text{ keV}}\right), & E_0 < h\nu < E_1 \\ B_3 p_\nu \left(\frac{h\nu}{E_1}\right)^{-1.6} \left[1 + q \left(\frac{h\nu}{1 \text{ keV}}\right)^{0.54}\right], & E_1 < h\nu < E_2 \\ B_4 p_\nu \left(\frac{h\nu}{E_2}\right)^{-1.28} \exp\left(\frac{-h\nu}{600 \text{ GeV}}\right), & h\nu > E_2 \end{cases} \quad (13)$$

where

$$p_\nu = S_k \exp\left(-\frac{1 \text{ keV}}{h\nu}\right), \quad q = 4.1 \times 10^{-3},$$

$$E_0 = 2 \text{ keV}, \quad E_1 = 113 \text{ keV} \quad \text{and} \quad E_2 = 100 \text{ MeV}.$$

Here the factor S_k has been adjusted to match the hard X-ray background measurements at $z = 0$. Its value depends on the value of assumed α . The S_k values for different α are also given in Table 1. The normalizations in equation (13) are

$$B_1 = A_3 \left(\frac{E_0}{12.4 \text{ eV}}\right)^\alpha \exp\left(\frac{E_0}{h\nu_a}\right), \quad B_2 = B_1 \exp\left(\frac{2}{83}\right),$$

$$B_3 = 9.246 \times 10^{-2} B_2 \quad \text{and} \quad B_4 = 5.444 \times 10^{-6} B_2.$$

Note that with these normalization factors (see B_1) along with the S_k , the type-2 QSO SED has been scaled with type-1 QSO emissivity. The form of type-2 QSO SED has been adopted from [Sazonov et al. \(2004\)](#) which we modified with different normalizations and a very high-energy part that reproduces the $z = 0$ X-ray and γ -ray background measurements up to TeV energies (see Section 4.3 and Fig. D3). Our type-2 QSO SED even includes γ -ray emission, therefore it serves as a combination of all high-energy emitting type of QSOs.

Note that, for GeV γ -rays our constructed SED is not the intrinsic SED because we ignored the effect of the EBL on their propagation. These γ -ray photons while traveling

Table 1. Parameters of QSO SED given by equation 12 and 13

Model Name	α	$h\nu_a$ (keV)	S_k
Q14	-1.4	40	0.4
Q15	-1.5	20	0.7
Q16	-1.6	8.0	1.0
Q17	-1.7	4.0	1.3
Q18	-1.8	2.0	1.3
Q19	-1.9	1.5	1.6
Q20	-2.0	1.0	1.4

Notes: Q18 is our fiducial model.

through the IGM get annihilated upon collision with the EBL photons via electron-positron pair-production. This phenomena provides an effective optical depth $\tau_\gamma(\nu, z)$ for γ -rays which were emitted at redshift z with frequency $\nu(1+z)$ and observed on earth with frequency ν . Therefore, in our formalism the intrinsic (rest-frame) SED of γ -ray blazars at redshift z should be $k_\nu^{Q2} e^{\tau_\gamma(\nu(1+z), z)}$. In Appendix B, we provide the values of $\tau_\gamma(\nu, z)$ from our EBL models which are mostly dominated by photons having energy lower than 10 eV and therefore insensitive to the value of assumed α or the QSO emissivity.

In the right-hand panel of Fig. 1, we show our full composite QSO SED which is an addition of k_ν^{Q1} and k_ν^{Q2} obtained for $\alpha = -1.8$. To obtain the QSO emissivity at $z = 0$ the full SED is normalized to the ϵ_{1000}^Q at $z = 0$. As shown in the figure, the type-1 QSOs contribute mainly at $E < 2$ keV, type-2 QSOs at $E > 2$ keV till MeV and blazars at higher energies. At H I and He II ionizing energies, contribution from type-2 QSOs is extremely small. Therefore, 912 \AA emissivity from all QSOs can be effectively written as

$$\epsilon_{912}^Q(z) = \left(\frac{1000}{912}\right)^\alpha \epsilon_{1000}^Q(z). \quad (14)$$

One can interpret the ratio k_ν^{Q2}/k_ν^{Q1} , which depends on choice of α , as the fraction of type-2 QSOs (including highly obscured Compton thick QSOs and γ -ray blazars), however such an interpretation is subject to the shape of X-ray SED assumed for type-1 QSOs. We have further discussed such an interpretation in Appendix C. We do not model QSO SED in infra-red (IR). This does not affect our background calculations since QSOs contribute negligibly to IR background (see also [Sazonov et al. 2004](#)). Galaxies are more important in the optical and IR wavelengths. We discuss the galaxy emissivity in the following subsection.

3.2 Galaxy Emissivity

The galaxy emissivity ϵ_ν^G is obtained by integrating the galaxy luminosity functions (GLFs). To obtain this at each ν from handful of GLF measurements, it is customary to use these GLFs to derive the star formation rate density (SFRD) first and then generate ϵ_ν^G at each ν using stellar population synthesis models. However, most of the star formation tracers, especially the far-UV luminosity function

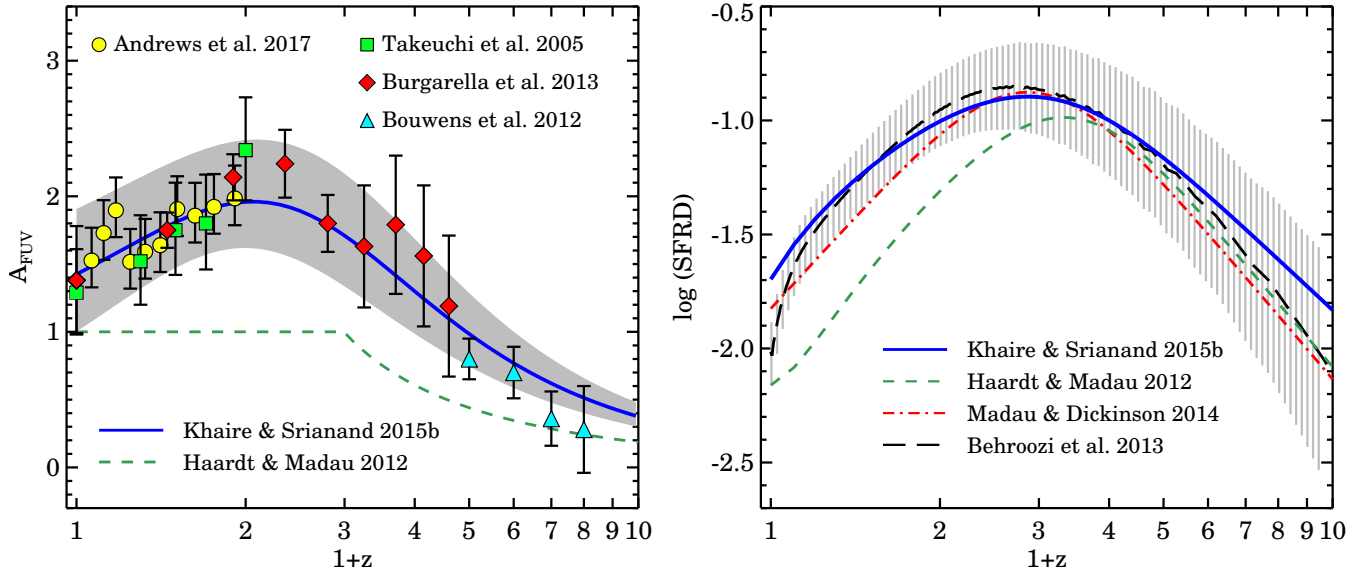


Figure 2. Left-hand panel: the average dust attenuation at FUV band (A_{FUV}) in magnitudes with z . The solid-curve shows $A_{\text{FUV}}(z)$ used in our EBL (equation 15) and the gray-shaded region shows the range in the $A_{\text{FUV}}(z)$ arising from the scatter in the FUV luminosity functions of the galaxies (KS15b). Measurements by Andrews et al. (2017, circles) are obtained by fitting SEDs of large number of galaxies. Data points from Takeuchi et al. (2005, squares) and Burgarella et al. (2013, diamonds) were obtained using IRX- β relation on IR and FUV luminosity functions of the galaxies. Bouwens et al. (2012, triangles) measurements used the slopes of high- z galaxy SEDs. We also show $A_{\text{FUV}}(z)$ used by HM12 (dash curve) for comparison. Right-hand panel: the SFRD(z) in units of $M_{\odot} \text{yr}^{-1} \text{Mpc}^{-3}$. The solid-curve shows our fiducial SFRD(z) obtained using the $A_{\text{FUV}}(z)$ shown in the left-hand panel (equation 16). For comparison we also show the SFRD estimated by Madau & Dickinson (2014, dot-dash curve), Behroozi et al. (2013, big-dash curve) and by HM12 (small-dash curve). The vertical-striped region shows the 1σ uncertainty in the SFRD(z) from Behroozi et al. (2013). At $z < 2$ HM12 SFRD(z) is significantly different from others.

which probes the most distant Universe, suffer from the unknown dust attenuation intrinsic to galaxies. The SFRD obtained using the far-UV GLFs is degenerate with the assumed amount of the dust attenuation in the FUV band (A_{FUV}). We addressed this issue in KS15b, where by using multi-wavelength GLFs we lifted the degeneracy between SFRD(z) and $A_{\text{FUV}}(z)$ for an assumed extinction curve. We found that for Large Magellanic Cloud Super-shell (LMC2) extinction curve (from Gordon et al. 2003), our predicted $A_{\text{FUV}}(z)$ is remarkably consistent with its measurements (see left-hand panel of Fig. 2) obtained using IRX- β relation on FUV and FIR GLFs (Takeuchi et al. 2005; Burgarella et al. 2013). The high- z extrapolated part of our $A_{\text{FUV}}(z)$ is also consistent with the $A_{\text{FUV}}(z)$ measurements obtained from the UV slopes of galaxies upto $z \sim 7$ (Bouwens et al. 2012). The $A_{\text{FUV}}(z)$ is crucial not only to get the background in UV-optical wavelengths but also in FIR which is mainly dominated by the dust re-emission from galaxies.

We use the $A_{\text{FUV}}(z)$ magnitudes and SFRD(z) from the KS15b obtained for LMC2 extinction curve. These are

$$A_{\text{FUV}}(z) = \frac{1.42 + 0.93z}{1 + (z/2.08)^{2.2}} \quad (15)$$

$$\text{SFRD}(z) = 10^{-2} \times \frac{2.01 + 8.48z}{1 + (z/2.5)^{3.09}} M_{\odot} \text{yr}^{-1} \text{Mpc}^{-3}. \quad (16)$$

To determine the $A_{\text{FUV}}(z)$ and SFRD(z) in KS15b, we integrated the compiled multi-wavelength GLFs down to $0.01L_{\nu_0}^*$ and used a stellar population synthesis code STAR-

BURST99 (Leitherer et al. 1999). It uses Salpeter initial mass function (IMF; Salpeter 1955) with exponent -2.35 and the stellar mass range from 0.1 to $100 M_{\odot}$ with a constant metallicity of 0.4 times the solar value (i.e., $Z = 0.008$).

In the left-hand panel of Fig. 2, we show our $A_{\text{FUV}}(z)$ (solid-curve) along with their independent measurements obtained using the IRX- β relation (Takeuchi et al. 2005; Burgarella et al. 2013; Bouwens et al. 2012). Our $A_{\text{FUV}}(z)$ is also remarkably consistent with the recent measurements by Andrews et al. (2017) obtained by fitting SEDs to large number of galaxies observed in GAMA and COSMOS surveys (see also, Driver et al. 2016a). The gray-shaded region shows the uncertainty in the obtained $A_{\text{FUV}}(z)$ arising from the scatter in the reported far-UV GLFs (see KS15b). For comparison, we also show $A_{\text{FUV}}(z)$ used in HM12 for their UVB calculations, which is significantly smaller than the measurements and our values. The difference in the $A_{\text{FUV}}(z)$ leads to different emissivities and SFRD(z) which can severely affect the estimates of the EBL as well as the required f_{esc} to be consistent with Γ_{HI} measurements. Our SFRD(z) obtained from the $A_{\text{FUV}}(z)$ and stellar population synthesis models is shown in the right-hand panel of Fig. 2. For comparison we also show the SFRD(z) obtained by HM12, Madau & Dickinson (2014) and Behroozi et al. (2013, scaled by factor 1.7 to match the differences in the IMF used). SFRD(z) of HM12 is significantly smaller than others due to the lower $A_{\text{FUV}}(z)$, as small as factor of ~ 3 at $z < 2$. At $z < 6$ our SFRD(z) agrees well with those of Behroozi et al. (2013) and Madau & Dickinson (2014) with differences smaller

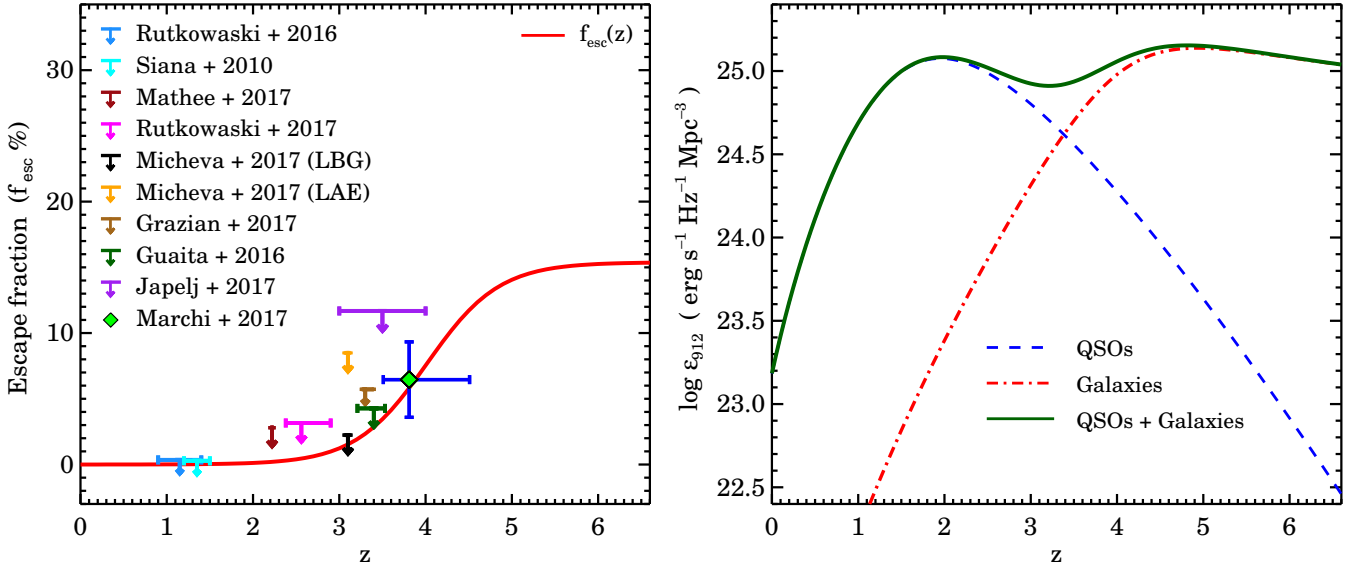


Figure 3. Left-hand panel: the average escape fraction $f_{\text{esc}}(z)$ of H I ionizing photons from galaxies used in our UVB code (solid-curve, equation 21). Various data points show the recent estimates of average f_{esc} where downward-arrows indicate 1σ upper limits. These points have been converted for our fiducial galaxy emissivity models as explained in the text and provided in Table A1. Horizontal bars on each point indicate the redshift range of the galaxy sample considered for measurements. Right-hand panel: the net specific emissivity at 912 Å (ϵ_{912}) with z used in our fiducial UVB model (solid curve). The panel also shows the contribution from QSOs (dash-curve, see equation 14 for $\alpha = -1.8$), galaxies (dot-dash curve, from equation 20 and 21 obtained for the $f_{\text{esc}}(z)$ shown in the left-hand panel) and the addition of both (solid curve).

than 0.1 and 0.2 dex, respectively. At $z > 6$ our SFRD(z) is more owing to higher $A_{\text{FUV}}(z)$, however, within the 1- σ uncertainty given by [Behroozi et al. \(2013\)](#) as shown by the striped region in the right-hand panel of Fig. 2 and also consistent with the SFRD(z) from very high- z GLFs ([Oesch et al. 2014; Bouwens et al. 2015; McLeod et al. 2015](#)).

We obtain the $\epsilon_{\nu}^G(z)$, using $A_{\text{FUV}}(z)$ and SFRD(z) from equation (15) and (16) in the following convolution integral

$$\epsilon_{\nu}^G(z) = C_{\nu}(z) \int_z^{\infty} \frac{\text{SFRD}(z') l_{\nu}[t(z) - t(z'), Z] dz'}{(1 + z') H(z')}, \quad (17)$$

where $l_{\nu}[t(z) - t(z'), Z]$ is a specific luminosity obtained from a simple stellar population in units of $\text{erg s}^{-1} \text{Hz}^{-1}$ per unit mass of stars formed having metallicity Z and age $t_0 = t(z) - t(z')$. The $C_{\nu}(z)$ is,

$$C_{\nu}(z) = \begin{cases} 10^{-0.4 A_{\text{FUV}}(z) \frac{D_{\nu}}{D_{\text{FUV}}}}, & \text{at } \lambda > 912 \text{ \AA} \\ f_{\text{esc}}(z), & \text{at } 228 < \lambda < 912 \text{ \AA} \\ 0, & \text{at } \lambda < 228 \text{ \AA}. \end{cases} \quad (18)$$

At $\lambda > 912 \text{ \AA}$, $C_{\nu}(z)$ is the dust correction where D_{ν}/D_{FUV} is the LMC2 extinction curve D_{ν} normalized at FUV band. We take $C_{\nu} = f_{\text{esc}}$ at $228 < \lambda < 912 \text{ \AA}$ which assumes that the ionizing photons are predominantly escaping through low-density low-dust channels in the galaxies ([Fujita et al. 2003; Paardekooper et al. 2011](#)) or these photons are mostly generated by unobscured runaway stars in the outskirts of galaxies ([Gnedin et al. 2008; Conroy & Kratter 2012](#)). Note that we are treating f_{esc} in the same way as previous UVB calculations (such as [HM12](#) and [FG09](#)) treated. We assume that no helium ionizing photons ($\lambda < 228 \text{ \AA}$) escape from galaxies. It is a reasonable assumption for galaxies at $z <$

6 since the stellar population generates a negligibly small amount of high energy photons in the absence of a large number of population III stars.

The $\epsilon_{\nu}^G(z)$ obtained by this method at $228 < \lambda < 912 \text{ \AA}$ can be approximated as a power-law

$$\epsilon_{\nu}^G(z) = \epsilon_{\nu_{912}}^G(z) \left(\frac{\nu}{\nu_{912}} \right)^{\beta}. \quad (19)$$

We find that $\beta = -1.8$ provides a best fit (see also [Becker & Bolton 2013](#)). We use this power-law approximation for simplicity, to speed up the UVB calculations, and to smooth out the small fluctuations in ϵ_{ν}^G produced by population synthesis models around $\sim 900 \text{ \AA}$. We also verify that this power-law with $\beta = -1.8$ reproduces the number of photons and the Γ_{HI} obtained by original ϵ_{ν}^G . A simple fit to the redshift evolution of our $\epsilon_{\nu_{912}}^G$ in units of $\text{erg s}^{-1} \text{Hz}^{-1} \text{Mpc}^{-3}$ is given by

$$\epsilon_{\nu_{912}}^G(z) = f_{\text{esc}}(z) \times 10^{25} \frac{3.02 + 13.12z}{1 + (z/2.44)^{3.02}}. \quad (20)$$

The extreme-UV emissivity from galaxies depends on the value of $f_{\text{esc}}(z)$. Therefore, an accurate estimate of this is required to model the UVB.

As mentioned in Section 1, only handful of galaxies are detected to show emission of extreme-UV photons in large sample of galaxies. Most of the average f_{esc} measurements are upper limits. Therefore, we resort to deduce the $f_{\text{esc}}(z)$ that is required to be consistent with the well-measured Γ_{HI} values as demonstrated in [Khaire et al. \(2016\)](#). We choose the $f_{\text{esc}}(z)$ to be

$$f_{\text{esc}}(z) = \frac{10^{-5}}{6.5 \times 10^{-5} + \exp(-2.4z)}, \quad (21)$$

which is consistent with the $f_{\text{esc}}(z)$ from [Khaire et al. \(2016\)](#)

and reproduce the $\Gamma_{\text{HI}}(z)$ measurements (see Section 4.1 and Fig. 4). In the left-hand panel of Fig. 3, we compare our $f_{\text{esc}}(z)$ with recent measurements from literature. The direct measurements of $f_{\text{esc}}(z)$ are obtained using the observed ratio of flux (f_{λ_i}) at some extreme-UV wavelength $\lambda_i \leq 912\text{\AA}$ to the flux $f_{\lambda_{\text{FUV}}}$ at some other higher wavelength, mostly in FUV band. To get the $f_{\text{esc}}(z)$ value, in addition to this observed ratio $f_{\lambda_i}/f_{\lambda_{\text{FUV}}}$, three other model dependent quantities are required. These are the intrinsic ratio $f_{\lambda_i}/f_{\lambda_{\text{FUV}}}$ obtained from stellar population synthesis of the assumed galaxy model, the dust attenuation $A_{\lambda_{\text{FUV}}}$ and the correction for the transmission through IGM ($e^{\tau_{\text{eff}}}$). We have corrected the measurements shown in Fig. 3 for our values of $A_{\lambda_{\text{FUV}}}$ and the intrinsic ratio $f_{\lambda_i}/f_{\lambda_{\text{FUV}}}$. For readers, these values are provided in Table A1. We have taken the same $e^{\tau_{\text{eff}}}$ used in the respective papers since, like us, most of them use the H I column-density distribution from Inoue et al. (2014). As shown in Fig. 3, our $f_{\text{esc}}(z)$ is consistent with the measurements claimed by Marchi et al. (2017) and all other 1σ upper limits (Siana et al. 2010; Guaita et al. 2016; Rutkowski et al. 2016, 2017; Matthee et al. 2017; Micheva et al. 2017; Grazian et al. 2017; Japelj et al. 2017). Following Khaire et al. (2016), in absence of any observational evidence for the evolution of f_{esc} at $z > 6$, our $f_{\text{esc}}(z)$ reaches a constant asymptotic value of 0.15. As shown later, this f_{esc} value gives H I reionization history consistent with various observations.

In the right-hand panel of Fig. 3, we show the relative contribution of galaxies and QSOs to the extreme-UV emissivities, in terms of $\epsilon_{912}(z)$. We show QSO contribution $\epsilon_{912}^Q(z)$ for $\alpha = -1.8$ and our galaxy contribution $\epsilon_{912}^G(z)$ (from equation 20 and 21). QSOs dominate the extreme-UV emissivity at $z < 3$ (irrespective of the assumed α value) and galaxies dominate at $z > 3.5$. The sharp increase and then saturation in $\epsilon_{912}^G(z)$ results from the $f_{\text{esc}}(z)$ adopted in our study (see the left hand panel of Fig. 3). The rapid decrease in the $\epsilon_{912}^Q(z)$ at $z > 3$ is the main reason for the required rapid increase in $f_{\text{esc}}(z)$ and hence in the $\epsilon_{912}^G(z)$ at $3.5 < z < 5.5$ in order to be consistent with the Γ_{HI} measurements (Khaire et al. 2016). If low luminosity AGNs contribute appreciably to the emissivity at $z > 3.5$, as claimed by Giallongo et al. (2015), one may not need such a rapid increase in $f_{\text{esc}}(z)$ (see e.g., Khaire et al. 2016). We discuss the effect on UVB arising from uncertainties in galaxy emissivity in Section 4.4.2.

The galaxy emissivity obtained using equation (17) does not provide the IR and FIR emissivities since it includes only stellar radiation. Radiation from old stellar population peaks in near-IR around $1-3\mu\text{m}$ and falls steeply at smaller wavelengths. Most of the observed FIR emission from galaxies originate from the thermal emission of interstellar dust heated by UV and optical light from stars. We take the FIR emissivity estimated by KS15b for the same $\text{SFRD}(z)$, $A_{\text{FUV}}(z)$ and the LMC2 extinction curve used here. It has been estimated under the assumption that the energy density absorbed by dust in UV and optical wavelengths is getting emitted in IR to FIR wavelengths and the spectral shape of this emission is similar to the one observed from galaxies in local Universe. Such a spectral shape has been taken from local IR galaxy templates of Rieke et al. (2009). This FIR emissivity has been shown to be consistent with

various local observations. For more details on this we refer readers to the section 5 of KS15b.

3.3 Diffuse Emissivity

Most of the gas in the IGM is in photoionization equilibrium with the UVB. This gas re-emits a fraction of energy it absorbs from the UVB at different wavelengths. This re-emission happens through various recombination channels such as Lyman-series and Lyman-continuum emission of H I, He I and He II, similarly for Balmer and higher order series and continuum. Although, it contributes negligibly to UVB as shown by FG09, we model few of the most dominant contributions in the extreme-UV wavelengths such as Lyman-continuum emission from H I and He II, Balmer-continuum emission from He II and the Lyman- α emission from He II. For modeling these, we follow the same procedure used by FG09 and HM12. We refer readers to the relevant sections in FG09 and HM12.

We have also modeled the H I Lyman- α emissivity from galaxies which is not included in the population synthesis models. For this we followed the simple procedure used by HM12 (their section 7.1), which assumes that 68% of the Lyman continuum photons which are not able escape the galaxies (i.e., $(1 - f_{\text{esc}}) \times 0.68$) are being emitted as Lyman- α photons. Unlike HM12, we multiply this H I Lyman- α emissivity by $10^{-0.4A_{\text{FUV}}(z)D_{Ly\alpha}/D_{\text{FUV}}}$ to capture the effect of the dust attenuation. Therefore, our UVB does not show prominent Lyman- α emission as compared to HM12. Note that such a simple method to estimate the H I Lyman- α emissivity may not be consistent with the complex radiative transfer of Lyman- α photons emitted by stellar population through ISM and CGM of galaxies (see e.g., Neufeld 1990, 1991; Dijkstra et al. 2006; Dayal et al. 2010; Gronke et al. 2016; Dijkstra 2017).

4 BASIC RESULTS

In this section we discuss basic results from our fiducial model (Q18 model with $\alpha = -1.8$ used in QSO SED) for the photoionization and photoheating rates of H I and He II, the reionization history of H I and He II, the spectrum of local EBL from FIR to γ -rays and the UVB spectrum along with its comparison with models of FG09 and HM12. Similar results for the models obtained with different α are presented in the Appendix D. We also discuss the uncertainties in the UVB arising from different model parameters.

4.1 Photoionization and photoheating rates

The photoionization rates of H I and He II are the only observed constraints on the UVB. Moreover, these are just integral constraints and can decide the intensity of the UVB if only the spectral shape of the UVB is known. However, unlike the direct observational constraints on EBL at wavelengths other than extreme-UV, photoionization rates are not limited to the local Universe and can be measured across a large redshift range using various observational techniques as mentioned in Section 1. In our analysis, we use the recent Γ_{HI} measurements obtained by comparing the cosmological simulations of the IGM to the observed

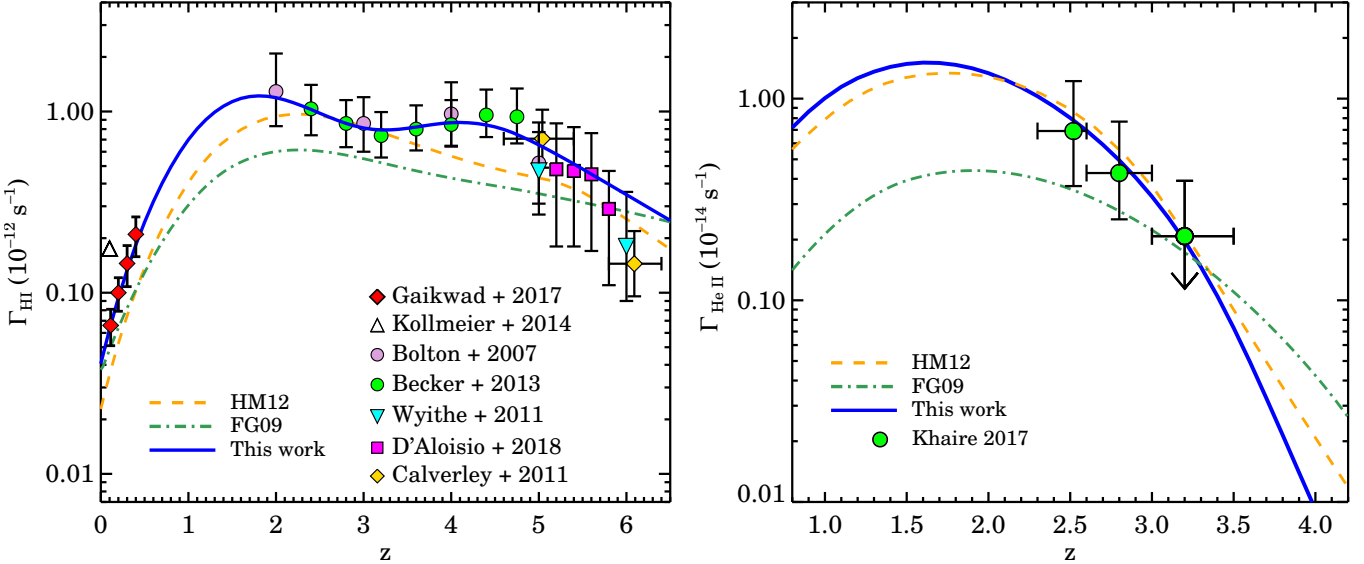


Figure 4. The photoionization rate of H I (Γ_{HI} ; left-hand panel) and He II ($\Gamma_{\text{He II}}$; right-hand panel) as a function of z from our fiducial UVB model (solid curves; see Fig. D1 for UVB models with different α). For comparison we show the Γ_{HI} from UVB models of HM12 (dash curve) and FG09 (dot-dash curve). Various data points in the left-hand panel show the recent measurements of Γ_{HI} . The $\Gamma_{\text{He II}}$ from Khaire (2017) is obtained by using the measurements of $\tau_{\alpha}^{\text{He II}}$ from Worseck et al. (2016).

statistics of the Ly- α forest by Gaikwad et al. (2017a) at $z < 0.5$, by Becker & Bolton (2013) and Bolton & Haehnelt (2007) at $2 < z < 5$, and by D’Aloisio et al. (2018) and Wyithe & Bolton (2011) at $5 < z < 6$. We also use the Γ_{HI} measurements obtained from proximity zones of high- z QSOs by Calverley et al. (2011) at $z = 5$ and 6.1. In addition to Γ_{HI} , we have also used the $\Gamma_{\text{He II}}$ measurements by Khaire (2017).

In the left-hand panel of the Fig. 4, we show the $\Gamma_{\text{HI}}(z)$ obtained from our fiducial UVB model along with various available measurements. The remarkable agreement between our prediction and the Γ_{HI} measurements at $z > 3$ is not surprising since we have chosen the appropriate $f_{\text{esc}}(z)$ to match these measurements (see Khaire et al. 2016). Whereas, at $z < 3$ the UVB is determined by our updated QSO emissivity alone (see also KS15a) and there is no need to adjust $f_{\text{esc}}(z)$. However, for making $f_{\text{esc}}(z)$ as a continuous function of z , we have taken negligibly small values of $f_{\text{esc}}(z)$ at $z < 0.5$. At $z < 0.5$, our Γ_{HI} is not only consistent with measurements from Gaikwad et al. (2017a) but also with Shull et al. (2015); Gurvich et al. (2017); Viel et al. (2017) and Fumagalli et al. (2017), which are not shown in the figure due to shortage of space. The $z = 0$ Fumagalli et al. (2017) measurement is obtained using the observations of H α fluorescence from a nearby faint disc galaxy. Note that all these $z < 0.5$ measurements provide ~ 2.5 times smaller Γ_{HI} than the measurements of Kollmeier et al. (2014). For comparison, we also show the $\Gamma_{\text{HI}}(z)$ obtained in UVB models of HM12 and FG09³. At $z < 0.5$, unlike our models these two models under-predict Γ_{HI} values compared to latest measurements. This is one of our major improvements over previous UVB models.

³ We use their December 2011 update available on web-page <http://galaxies.northwestern.edu/>

The differences in the $\Gamma_{\text{HI}}(z)$ predicted by these models at $z > 2$ are because of choosing different inputs in their UVB models, such as f_{esc} , in order to be consistent with different $\Gamma_{\text{HI}}(z)$ measurements. For example, FG09 tried to be consistent with $\Gamma_{\text{HI}}(z)$ from Faucher-Giguère et al. (2008) whereas HM12 with $\Gamma_{\text{HI}}(z)$ from Becker et al. (2007), which are quite different from the recent measurements (see Becker & Bolton 2013, for more details). Overall, our $\Gamma_{\text{HI}}(z)$ values are in excellent agreement with their recent measurements at all redshifts than previous UVB models.

UVB models with different α give slightly different values of Γ_{HI} at $z < 3$ because at these redshifts the UVB is dominated by QSOs. However, these are still consistent with the measurements of Gaikwad et al. (2017a) as shown in the left-hand panel of Fig. D1 in the Appendix. This shows that the difference in the obtained Γ_{HI} due to changing α (from -1.4 to -2) is smaller than the present uncertainties on the low- z Γ_{HI} measurements. At $z > 3$ the Γ_{HI} is dominated by galaxy emissivity therefore left-hand panel of Fig. D1 does not show any change in Γ_{HI} with α .

In the right-hand panel of the Fig. 4, we show the $\Gamma_{\text{He II}}(z)$ obtained from our fiducial UVB along with the values determined in Khaire (2017) at $2.5 < z < 3.5$ by using the He II effective optical depth measurements of Worseck et al. (2016) and the $f(N_{\text{HI}}, z)$ from Inoue et al. (2014). For comparison, we also show the $\Gamma_{\text{He II}}(z)$ from UVB models of HM12 and FG09. $\Gamma_{\text{He II}}(z)$ obtained by our and HM12 UVB models match very well with the measurements. Even the $\Gamma_{\text{He II}}(z)$ from FG09 within this z -range, where direct observations are available, is broadly consistent with these measurements. The agreement between our and HM12 $\Gamma_{\text{He II}}$ at $2.5 < z < 3.5$, despite the fact that we are using different input parameters, is mostly coincidental and because of using different QSO SEDs. HM12 used smaller ϵ_{1000}^Q but steeper SED ($\alpha = -1.57$) on the other hand we used higher ϵ_{1000}^Q but shallower SED ($\alpha = -1.8$). Also, the fact that both

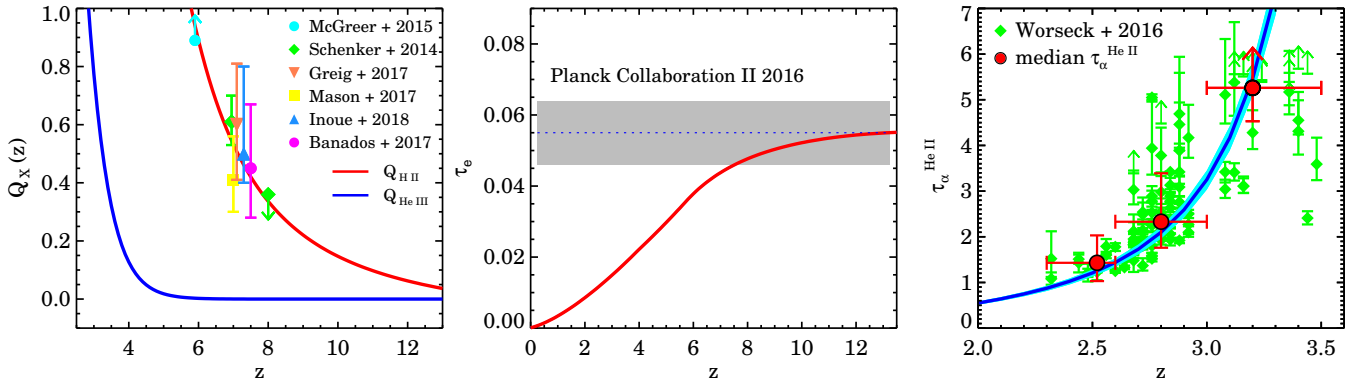


Figure 5. *Left-hand panel:* volume filling fraction of H II (red curve) and He III (blue curve) obtained for our fiducial UVB model. For comparison the Q_{HII} measurements from Schenker et al. (2014); McGreer et al. (2015); Greig et al. (2017); Mason et al. (2017); Bañados et al. (2017); Inoue et al. (2018) has been shown. We get $z_{\text{re}} = 5.8$ for H I and $z_{\text{re}} = 2.8$ for He II. *Central panel:* electron scattering optical depth (τ_e) obtained from our fiducial UVB model (solid curve) shown together with the measurements from Planck Collaboration et al. (2016b, dotted line with gray shade). *Right-hand panel:* the He II Lyman- α effective optical depth ($\tau_{\alpha}^{\text{He II}}$) obtained from our fiducial UVB model (solid curves with $b = 28 \text{ km s}^{-1}$ and cyan shade obtained by changing b from 24 to 32 km s^{-1}) with the measurements from Worseck et al. (2016, diamonds). The red points show the median $\tau_{\alpha}^{\text{He II}}$ in redshift bins indicated by horizontal bars.

models get almost the same $\Gamma_{\text{H I}}$ within $2.5 < z < 3.5$ helps in getting the $\Gamma_{\text{He II}}(z)$ agreement.

The $\Gamma_{\text{He II}}$ is more sensitive to the value of α than $\Gamma_{\text{H I}}$. It is because α is obtained by normalizing QSO emissivity at $\lambda = 1000 \text{ \AA}$. Therefore, a small change in α results in a large change for He II ionizing photons at more than four times smaller wavelengths. We show $\Gamma_{\text{He II}}$ obtained from our UVB models with different α in the right-hand panel of Fig. D2. Only $-2.0 < \alpha < -1.6$ are consistent with the $\Gamma_{\text{He II}}$ measurements and He II effective optical depths (for more detailed analysis on this refer to Khaire 2017).

In Table D1 we provide the photoionization and photoheating rates for H I, He I and He II from our fiducial UVB model with $\alpha = -1.8$ and in Tables D2-D7 for UVB models with different α . Photoheating rates for different species x are obtained by

$$\xi_x(z) = \int_{\nu_x}^{\infty} d\nu \frac{4\pi J_{\nu}(z)}{h\nu} h(\nu - \nu_x) \sigma_x(\nu). \quad (22)$$

In Fig. D2 we show the $\xi_{\text{HI}}(z)$ and $\xi_{\text{HeII}}(z)$ for our UVB models obtained with different values of α . The photoheating rates follow broadly the similar redshift evolution as photoionization rates (compare Fig. D1 and D2). As in the case for $\Gamma_{\text{He II}}$, the ξ_{HeII} is also sensitive to the value of α . Note, by construct, all these models consistently reproduce $\Gamma_{\text{H I}}(z)$ but differ only in $\Gamma_{\text{He II}}(z)$.

4.2 H I and He II reionization

We have calculated the H I and He II reionization history for the H I and He II ionizing emissivity used in our fiducial UVB model. The redshift evolution of volume filling factor Q_x of H II and He III are obtained by solving (see Madau et al. 1999; Khaire et al. 2016),

$$Q_x(z_0) = \frac{1}{\langle n \rangle} \int_{z_0}^{\infty} dz \frac{\dot{n}_y(z)}{(1+z)H(z)} \times \exp \left[-\alpha_y^B(T) \langle n \rangle \int_{z_0}^z dz' \frac{\chi(z')C(z')(1+z')^2}{H(z')} \right]. \quad (23)$$

where, $\langle n \rangle = \langle n_{\text{H}} \rangle$ and $y = \text{H I}$ when x is H II and $\langle n \rangle = \langle n_{\text{He}} \rangle$ and $y = \text{He II}$ when x is He III, $\dot{n}_y(t)$ is the comoving number density of ionizing photons per unit time for species y , $C(z)$ is the clumping factor and $\chi(z)$ is number of photoelectrons per hydrogen atom at redshift z . We use $\chi(z) = 1.083$ at $z > 4$ and $\chi(z) = 1.16$ at $z < 4$ assuming that within the regions where H I is ionized the helium is predominantly singly ionized at $z > 4$ and doubly ionized at $z < 4$. We use the comoving number density of hydrogen $\langle n_{\text{H}} \rangle = 1.87 \times 10^{-7} \text{ cm}^{-3}$ and helium $\langle n_{\text{He}} \rangle = \langle n_{\text{H}} \rangle y_p / (4 - 4y_p)$ where $y_p = 0.248$ is the helium mass fraction from Planck Collaboration et al. (2016a). The $\dot{n}_y(z)$ is obtained by

$$\dot{n}_y(z) = \int_{\nu_y}^{\infty} d\nu \frac{\epsilon_{\nu}(z)}{h\nu}, \quad (24)$$

where ν_y is threshold ionization frequency for species y . We use clumping factor $C(z) = 9.25 - 7.21 \log(1+z)$ obtained from the cosmological hydrodynamical simulations of the IGM from Finlator et al. (2012).

We show the $Q_{\text{HII}}(z)$ and $Q_{\text{HeIII}}(z)$ results in the left-hand panel of Fig. 5. We also show recent measurements of Q_{HII} . H I reionization in our model completes at $z = 5.8$ (z at which $Q_x(z) = 1$) consistent with high- z Lyman- α forest observations (Becker et al. 2001; Fan et al. 2006). Our $Q_{\text{HII}}(z)$ is in agreement with lower limits from McGreer et al. (2015) obtained using dark-pixel statistics of high- z QSO spectra and with measurements of Greig et al. (2017) and Bañados et al. (2017) obtained using Lyman- α damping wings of two highest redshift QSOs. Our $Q_{\text{HII}}(z)$ is also consistent with the measurements obtained from the diminishing population of high- z Lyman- α emitters obtained by Schenker et al. (2014), Mason et al. (2017) and Inoue et al. (2018). We calculate the electron scattering optical depth τ_e of CMB (Eq. 12 from Khaire et al. 2016). The $\tau_e(z)$ from our reionization model is shown in the central panel of Fig. 5, which reaches asymptotic value $\tau_e = 0.55$ consistent with the measurements of Planck Collaboration et al. (2016b). This reiter-

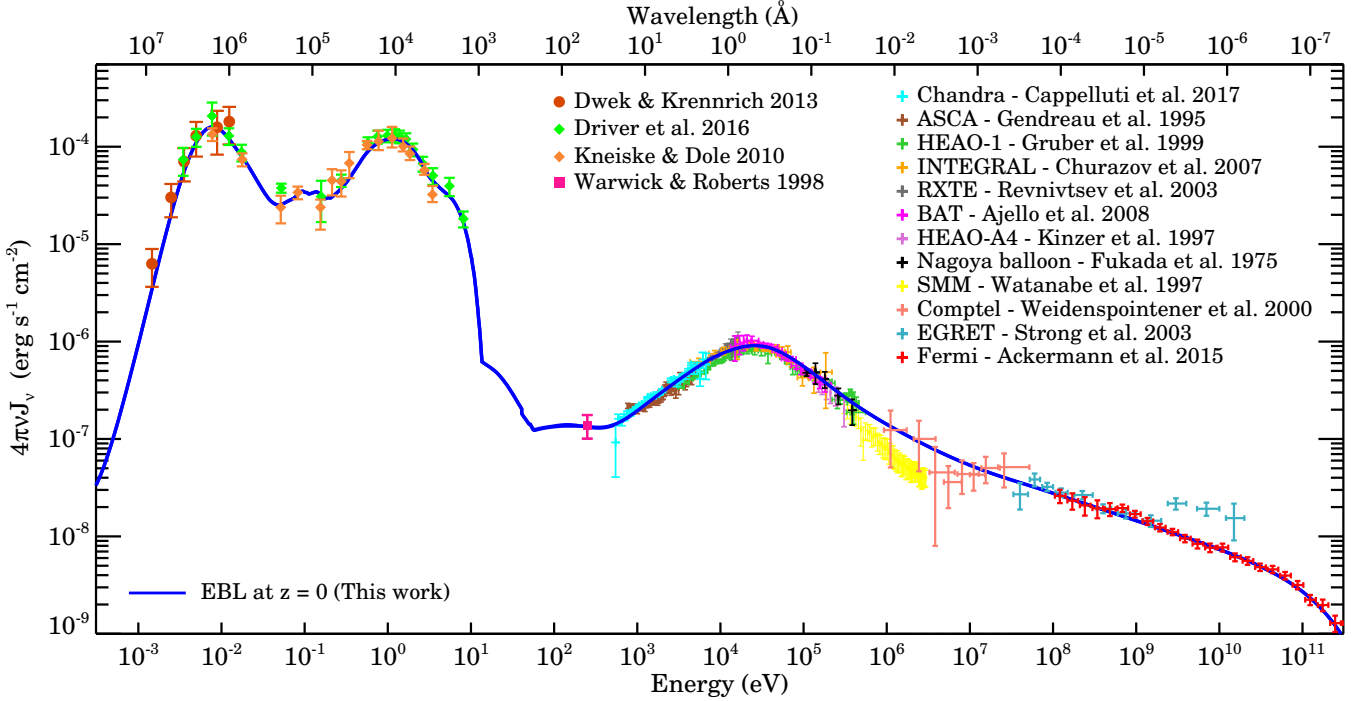


Figure 6. The intensity of $z = 0$ EBL from FIR to TeV γ -rays from our fiducial model (see Fig. D3 for EBL models with different α). Various measurements shown in the figure are summarized in Section 4.3.

ated the results of Khaire et al. (2016) that new constraints on H I reionization does not require $f_{\text{esc}}(z)$ at $z > 6$ to have a steep evolution and a constant value, such as 0.15 used here (equation 21), is sufficient to produce the consistent τ_e . The H I reionization history is same for all of our UVB models obtained with different α because in these models the H I reionization is driven by galaxies and QSOs contribute negligibly.

He II reionization in our fiducial model with $\alpha = -1.8$ completes at $z = 2.8$. It is consistent with various measurements of He II Lyman- α effective optical depths ($\tau_{\alpha}^{\text{He II}}$; Kriss et al. 2001; Shull et al. 2004, 2010; Fechner et al. 2006; Worseck et al. 2011, 2016), measurements of peak in the redshift evolution of mean IGM temperature (Becker et al. 2011; Hiss et al. 2017) and also with theoretical models of He II reionization (McQuinn et al. 2009; Compostella et al. 2013; La Plante & Trac 2016). We also consistently reproduce $\tau_{\alpha}^{\text{He II}}$ from Worseck et al. (2016), as shown in the right-hand panel of Fig. 5. It shows $\tau_{\alpha}^{\text{He II}}$ calculated from our fiducial UVB model (using equation 9 and 10 from Khaire 2017) for an assumed Doppler broadening $b = 28$ km/s with blue curve and the shaded cyan region provides values encompassed by changing b from 24 to 32 km/s. The red data points, shown to guide the eyes, are the median values of $\tau_{\alpha}^{\text{He II}}$ (within 95 percentile errors) as obtained in three different z bins (see table 2 of Khaire 2017). Note that the He II reionization history and $\tau_{\alpha}^{\text{He II}}(z)$ depends on the value of α . As shown in Khaire (2017), only $-2.0 < \alpha < -1.6$ are consistent with both $\tau_{\alpha}^{\text{He II}}$ measurements and epoch of He II reionization being $2.6 < z < 3.0$.

4.3 The EBL spectrum

In Fig. 6, we show our full EBL spectrum at $z = 0$. Our calculations cover more than fifteen orders of magnitude range in wavelength from FIR to TeV energy γ -rays. The three distinct peaks in the intensity, $4\pi\nu J_{\nu}$ in units of $\text{erg s}^{-1} \text{cm}^{-2}$, can be readily seen. These are the FIR peak arising from the dust emission around $\sim 100 \mu\text{m}$ (10^6\AA), the near IR peak dominated by old stellar population around $\sim 1 \mu\text{m}$ (10^4\AA) and the hard X-ray peak from type-2 QSOs around $\sim 30 \text{ keV}$ (0.4\AA). In general, the $\lambda > 912 \text{\AA}$ part of the EBL is dominated by emission from galaxies including their stellar and dust emission, the $\lambda < 228 \text{\AA}$ part is contributed by radiation only from QSOs, and the $912 > \lambda > 228 \text{\AA}$ part is contributed by both galaxies and QSOs. Relative contribution to the latter is determined by f_{esc} , which at $z = 0$ is negligibly small therefore it is contributed by QSOs alone.

In Fig. 6, we also show $z = 0$ EBL measurements at different wavelengths obtained by various methods and instruments. In the FIR wavelengths we use compiled measurements by Dwek & Krennrich (2013, their table 7) obtained from COBE. In the optical to FIR wavelengths we use compiled measurements by Kneiske & Dole (2010) and Driver et al. (2016b) obtained from integrated light from resolved galaxies in deep surveys. Our EBL models agree very well with these measurements. At 0.25 keV ($\lambda \sim 50 \text{\AA}$) the measurement are taken from Warwick & Roberts (1998) obtained using shadow measurements from ROSAT. The X-ray background measurements are taken from various instruments; Chandra (Cappelluti et al. 2017), ASCA (Gendreau et al. 1995), HEAO-1 and HEAO-4 (Gruber et al. 1999; Kinzer et al. 1997), Integral (Churazov et al. 2007), RXTE (Revnivtsev et al. 2003),

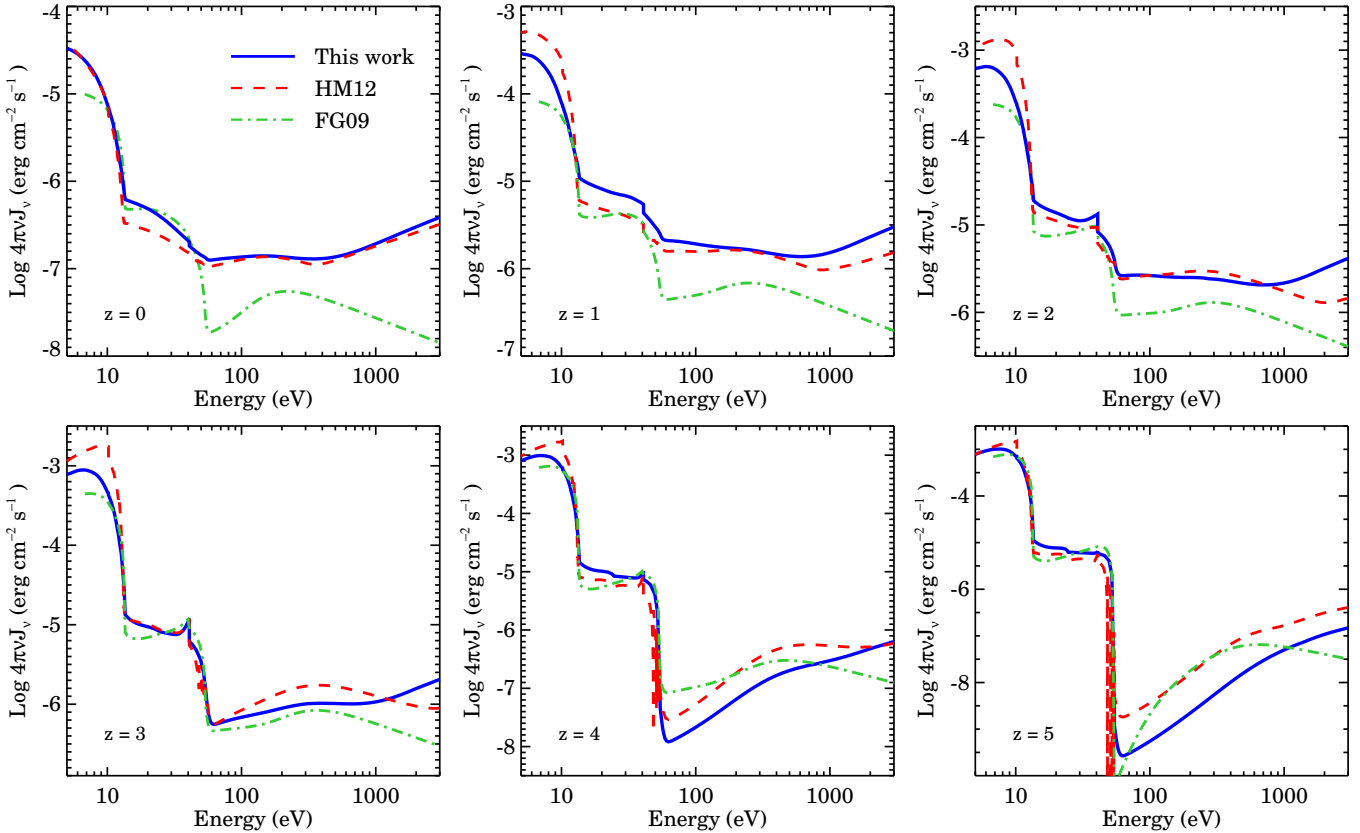


Figure 7. The spectrum of our fiducial UVB with energy (from 5 to 3000 eV) at $z = 0, 1, 2, 3, 4$ and 5 . The solid blue curve shows our fiducial UVB model (see Fig. D4 for UVB models with different α). The red dash and green dot-dash curves show the UVB models from HM12 and FG09.

Swift/BAT (Ajello et al. 2008) and Nagoya balloon (Fukada et al. 1975). Similarly γ -ray background measurements are taken from instruments: SMM (Watanabe et al. 1997), compton/Comptel (Weidenspointner et al. 2000), compton/EGRET (Strong et al. 2003) and Fermi/LAT (Ackermann et al. 2015). Our local fiducial EBL shows remarkable match with the X-ray and γ -ray background measurements all the way upto TeV γ -rays. It is not surprising, since we have constructed type-2 QSO and blazar SED (Section 3.1) and adjusted the normalizations (see Table 1) to do so. In Fig. D3, we show our EBL models with different values of α . The normalization $h\nu_0$ and S_k are taken such that despite different α , the local EBL will consistently reproduce the X-ray and γ -ray measurements as shown in the Fig. D3. However, with our assumed QSO SED shape it becomes difficult for models with $\alpha > -1.5$, to match few of the soft X-ray measurements.

The optical depth encountered by high-energy γ -rays (τ_γ) due to EBL are discussed in Appendix B. We find that the τ_γ is insensitive to EBL at $E < 10$ eV and thus to values of α . Note that, the EBL at $E < 10$ eV is same as the fiducial model given in KS15b (the median LMC2 model) and therefore it is consistent with many published models of optical and FIR EBL (e.g., Inoue et al. 2013; Gilmore et al. 2012; Finke et al. 2010; Kneiske & Dole 2010; Franceschini et al. 2008; Domínguez et al. 2011; Helgason & Kashlinsky 2012; Scully et al. 2014) as shown in the KS15b. We provide the

updated τ_γ values calculated for our fiducial EBL model including CMB.

The UVB at $z=0$, a part of the EBL at $50 < \lambda < 1200$ Å (i.e., $10 < E < 250$ eV) shown in Fig. 6, does not have any direct measurements. The measurements such as photoionization rates provide only integral constraints. Our models are consistent with them across a large z -range as shown in Fig. 4. Below we discuss the UVB spectrum and its redshift evolution in comparison with the previous UVB models. For the discussions hereafter, let us naively divide the EBL at $\lambda < 912$ Å ($E > 13.6$ eV) into three parts, the H I ionizing UVB at $13.6 < E < 54.4$ eV, the He II ionizing UVB at $54.4 < E < 500$ eV and the X-ray background at $E > 500$ eV.

In Fig. 7, we compare our fiducial UVB spectrum from $z = 0$ to 5 with the UVB from FG09 and HM12. Two distinct features in the UVB spectrum can be readily seen, these are ionization edges of H I (at 13.6 eV) and He II (at 54.4 eV). The smoothness of these features at the bottom of the troughs is because of the inclusion of Lyman continuum emission from H I and He II in UVB calculations. Also there is a small kink at 40.8 eV, prominent at $z = 1$ to 4 UVB, due to He II Lyman- α recombination emission. Another such small kink due to H I Lyman- α recombination emission from galaxies at 10.2 eV can be seen in HM12 but not in our UVB because this emission is suppressed in our models due to dust correction which is not performed by HM12 on this emission. FG09 do not include H I Lyman- α

recombination emission in their calculations. A sharp saw-tooth features due to Lyman series absorption of He II, seen in **HM12** UVB at $z > 3$, are not included in our and **FG09** models. Note that this saw-tooth modulation only shows significant difference in UVB at high redshifts and affects a very small wavelength range.

The differences in the UVB models can be roughly mapped to the differences in their predictions of $\Gamma_{\text{H}\,\text{I}}$ and $\Gamma_{\text{He}\,\text{II}}$ (see Fig. 4). The UVB model of the **FG09** is significantly different than our and **HM12** model at all wavelengths and redshifts. Our UVB model at $z < 2$ has higher H I ionizing UVB as compared to both **FG09** and **HM12** models. At $z < 1$, the similar He II ionizing UVB seen for ours and **HM12** model is because of the coincidental combinations of different α and ϵ_{ν}^C used in both models. At higher redshifts our He II ionizing UVB shows larger deviation from **HM12**. The similarity of X-ray background in our and **HM12** at $z = 0$ is due to the fact that both models match the X-ray background measurements, which was not attempted by **FG09**. The He II ionizing UVB in **FG09** shows comparatively smaller intensities with larger troughs at $z < 2$, suggesting that He II is recombining quickly in their model. This is not surprising given the small recombination time scales of the He II, the ever decreasing $\Gamma_{\text{He}\,\text{II}}$ at $z < 2$ and their small values at higher $z > 2$ (see right-hand panel of Fig. 4). Sources of all these significant differences among the three UVB models are the differences in the input parameters used in modeling, mainly the emissivities from QSOs and galaxies along with the $\Gamma_{\text{H}\,\text{I}}$ measurements that are used to check or calibrate the models.

The significant differences in the UVB models highlight the need for routinely updating the models using ever improving measurements of important input parameters. It is also important that the photoionization calculations which depend extensively on the assumed UVB model should use updated UVB keeping in mind all the uncertainties involved in the calculations of UVB. This is the main reason we provide six other UVB models having different α values than our fiducial model. For these models, the differences in the obtained UVB spectrum can be seen from Fig. D4 of Appendix. The intensity of He II ionizing UVB increases with α at all z since it depends only on QSO emissivity, on the other hand the H I ionizing UVB depends on both QSOs and galaxies therefore it only shows clear dependences on α for $z < 3$ where QSOs are dominating the UVB. As mentioned earlier, the intensity of He II ionizing UVB is more sensitive to α than H I ionizing UVB, as can be seen from Fig. D4 of Appendix for UVB at $z < 3$. We make all these UVBs publicly available for testing the dependence of photoionization calculation results on the assumed spectral shape of the UVB and to be able to quantify the uncertainties in the inferred quantities from these calculations. In the following section we give a detailed account of the uncertainties involved in the UVB calculations.

4.4 Uncertainties and caveats in the UVB models

The synthesis models of EBL are affected by several assumptions and many uncertainties arising from various input parameters. Here, we discuss such uncertainties and caveats in our UV and X-ray background models ($E > 13.6$ eV). We refer interested readers to Section 9 of **KS15b** for the dis-

cussion related to uncertainties in the far-UV to FIR parts ($E < 13.6$ eV) of the EBL.

4.4.1 QSO emissivity and SED

Uncertainties in QSO emissivity arises from how well we measure the QSO luminosity function (especially at low luminosities) and how representative is the SED used in the wavelength range where there are no direct observations. At $z < 2$ the QLFs are relatively well measured having shallow faint end slopes. Therefore, uncertainties in the obtained emissivity at $z < 2$ by integrating down to faintest luminosity is small. For example, for $z < 2$ QLFs from [Croom et al. \(2009\)](#) and [Palanque-Delabrouille et al. \(2013\)](#), changing the minimum luminosity $L_{\nu}^{\text{min}} = 0.01L^*$ to $L_{\nu}^{\text{min}} = 0$ changes the emissivity by less than 5%. Although we are using most recent measurements, the $z > 3$ QLFs at the low-luminosities are not well-measured which can make our assumed emissivities highly uncertain at these redshifts.

For a fixed type-1 QSO SED, any effect of a change in QSO emissivity will be compensated by a corresponding change in the f_{esc} to match the $\Gamma_{\text{H}\,\text{I}}$ measurements. However, this required change in f_{esc} can affect the spectral shape of the H I ionizing UVB depending on the differences in the type-1 QSO SED and the intrinsic SED of galaxies at $E > 13.6$ eV. Latter is obtained from stellar population synthesis models. For our fiducial UVB model, since the SED of QSOs (with $\alpha = -1.8$) is co-incidently same as our intrinsic SED of galaxies, using different QSO emissivity will not affect even the spectral shape of H I ionizing UVB. However, the He II ionizing UVB will be affected since it depends on the emission from type-1 QSOs and the $\Gamma_{\text{H}\,\text{I}}$ through radiative transfer effects that determine η (see [Khaire 2017](#))⁴. For example, there is no need to have seemingly unrealistic sharp increase in f_{esc} with z (the left-hand panel of Fig. 3) if the QSO emissivity is significantly higher than our fiducial values at $z > 3.5$. A much slower or no evolution in $f_{\text{esc}}(z)$ can be easily achieved as shown in [Khaire et al. \(2016\)](#) when one uses high QSO emissivity models based on the QLF measurements by [Giallongo et al. \(2015\)](#). However, such models have serious problems to reproduce the He II optical depth as a function of z ([Khaire 2017](#)). Moreover QLF measurements of [Giallongo et al. \(2015\)](#) are not supported by other similar studies (see e.g., [Weigel et al. 2015](#); [Ricci et al. 2017](#); [McGreer et al. 2017](#)).

Even the latest measurements of type-1 QSO SED show large variation in the measured value of power-law index α at $E > 13.6$ eV (from -2.3 to -0.5 within 1- σ errors; [Stevans et al. 2014](#); [Lusso et al. 2015](#); [Tilton et al. 2016](#)). See table 1 of [Khaire \(2017\)](#) for a summary of α measurements till date. The change in H I ionizing UVB arising due to change in α can be seen in Fig. D4 for $z \leq 2$ where the UVB is dominated by only type-1 QSOs. At $z > 3$, Fig. D4 shows no variation in H I ionizing UVB with change in α since it is dominated by emission from galaxies. The He II ionizing part of the UVB, however shows a large variation with α at all redshifts, since it only depends on type-1 QSO emissivity. The existing measurements of α

⁴ The change in f_{esc} can affect the He II ionizing UVB but only if the $\Gamma_{\text{H}\,\text{I}}$ is allowed to vary ([Khaire & Srianand 2013](#)).

probe smallest wavelength only upto 425 Å (30 eV), therefore there are no direct observational constraints on QSO SED at He II ionizing wavelengths. It has been assumed that the type-1 QSO SED at $\lambda < 912$ Å (E>13.6 eV) follows a single power law (with same α) which is normalized at 912 Å or higher wavelengths. This extrapolated power law to He II ionizing wavelengths gives large intensity differences corresponding to small changes in α . Therefore, He II ionizing UVB and $\Gamma_{\text{HeII}}(z)$ are more sensitive to α values than the H I ionizing UVB and $\Gamma_{\text{H1}}(z)$ as can be observed from Fig. D1 and D4 of Appendix. Under the assumption of a single power-law, in [Khaire \(2017\)](#) we find that α can have values from -1.6 to -2.0 consistent with measurements of [Lusso et al. \(2015\)](#) but smaller than measurements of [Stevans et al. \(2014\)](#) and [Tilton et al. \(2016\)](#). We provide UVB models with varying α from -1.4 to -2.0 in Appendix D. Using different α in the UVB models can affect the inferred properties of absorbers in the IGM and CGM, such as metallicity ([Hussain et al. 2017; Muzahid et al. 2017](#)), density ([Hussain et al. 2017; Upton Sanderbeck et al. 2017](#)) and temperatures.

Type-2 QSO SED and its normalizations, for different values of α used in type-1 QSO SED (see Table 1), are adjusted to be consistent with most of the X-ray and γ -ray background measurements at $z = 0$. These models with different α are shown in Fig. D3. For large values of α , such as -1.4 or -1.5, it is difficult to adjust normalizations to be consistent with some of the soft X-ray measurements. Nevertheless, all models are consistent with measurements at energies more than 20 keV all the way upto TeV. Although, this shows a major success of such type-2 QSO and blazar SED formulation, it has been assumed to scale with type-1 QSO emissivity, with the same scaling at all redshifts. Such scaling can be justified using recent observations of QSO population ([Lusso et al. 2013; Georgakakis et al. 2017; Vito et al. 2017](#)), where the fraction of type-2 QSOs is shown to be non-evolving with redshift (however, see [Liu et al. 2017; Gohil & Ballantyne 2017](#)). Due to this scaling, all the uncertainties in type-1 QSO emissivity reflect in the normalization of type-2 QSO SED. Although, it will not affect the obtained X-ray background it will change the interpretation related to the fraction of type-2 QSOs as discussed in the Appendix C. However, one should take such an interpretation with caution since the type-1 and type-2 QSO SEDs at X-ray can be adjusted arbitrarily to give different fractions of type-2 QSOs while still being consistent with local X-ray and γ -ray background measurements.

The soft-X ray background ($0.3 \text{ keV} < E < 2 \text{ keV}$) in our EBL model is contributed only by QSOs. However, as shown in [Upton Sanderbeck et al. \(2017\)](#), a significant contribution at $z \sim 0$ can come from hot intra-halo gas. The contribution from interstellar gas, CGM and X-ray binary is relatively small, however it depends on the SFRD used in the models. [Upton Sanderbeck et al. \(2017\)](#) used SFRD from [HM12](#) which is a factor of ~ 3 smaller than other estimates at $z < 1$. In our EBL models we have not included soft-X ray background arising from these different sources which when included in EBL models can further constrain the SED of type-1 and 2 QSOs and can also change the interpretation of fraction of type-2 QSOs as mentioned above.

4.4.2 Galaxy emissivity and escape fraction

The emissivity of galaxies at $\lambda < 912$ Å depends, in addition to the intrinsic emissivity, on the f_{esc} . In our model by construct f_{esc} is constrained to reproduce the H I ionizing UVB consistent with Γ_{H1} measurements. The intrinsic emissivity at $\lambda < 912$ Å depends on the derived SFRD and A_{FUV} as well as several parameters in the stellar population models. The derived SFRD and A_{FUV} alone can have systematic uncertainties of the order of 30% arising due to scatter in various FUV galaxy luminosity functions (see e.g., figures 1 and 5 of [KS15b](#)). Uncertainties arising in SFRD and A_{FUV} from different parameters in stellar population models, such as using different metallicity are smaller than this uncertainty (see section 8.2 of [KS15b](#) for more details).

As long as the intrinsic SED of galaxies at $\lambda < 912$ Å is same, the intensity of H I ionizing UVB remains same for different inferred values of f_{esc} arising from different values of SFRD, A_{FUV} , IMF, metallicity, or other parameters in the stellar population model. This is because in the UVB calculations the intrinsic galaxy SED has been scaled with f_{esc} (see also [HM12; FG09](#)), in absence of any observational constraints on the SED of emitted light from galaxies at $\lambda < 912$ Å. Such a scaling is justified under the assumption that these photons escape through gas and dust free channels, as proposed in many theoretical models (e.g., [Fujita et al. 2003; Gnedin et al. 2008; Paardekooper et al. 2011; Conroy & Kratter 2012](#)). Although, the intrinsic SED at $\lambda < 912$ Å, shows reasonably small variations for different properties of stellar populations such as metallicity (see section 4 of [Becker & Bolton 2013](#)) and different synthesis models (see section 9 of [HM12](#)), different IMFs can provide quite different intrinsic SEDs.

If independent constraints on f_{esc} are available then the above mentioned uncertainties will translate to uncertainties in the UVB spectrum. In our models, for a given QSO emissivity, the f_{esc} values are adjusted to match Γ_{H1} measurements in the absence of strong constraints on the f_{esc} measurements. In future, independent constraints on f_{esc} or H I ionizing emissivity will be useful to quantify the contributions of sources other than QSOs and galaxies to the UVB.

4.4.3 H I distribution and other uncertainties

The column density distribution of the H I, $f(N_{\text{HI}}, z)$ plays an important role in shaping the UVB model. The $f(N_{\text{HI}}, z)$ affects UVB estimate through the calculation of τ_{eff} , especially at $15 < \log(N_{\text{HI}} \text{ cm}^{-2}) < 20.5$ for H I ionizing UVB (see Fig. 8) and $\eta/4$ times smaller values for He II ionizing UVB. This N_{HI} range has relatively higher measurement uncertainty as compared to $\log(N_{\text{HI}} \text{ cm}^{-2}) < 14$ or > 20 due to saturation of the Lyman- α absorption. We have used a $f(N_{\text{HI}}, z)$ fitting form provided by [Inoue et al. \(2014\)](#) because it has been obtained by fitting a large number of different observations covering large redshift and N_{HI} range, as mentioned in Section 2. For comparison, in the left-hand panel of Fig. 8, we show the $f(N_{\text{HI}}, z)$ measurements at $z = 2.5$ along with the fitting forms from [Inoue et al. \(2014\)](#), [FG09](#) and [HM12](#). The fit from [Inoue et al. \(2014\)](#) is better than others at all N_{HI} . The difference in the obtained τ_{eff} at each N_{HI} for different

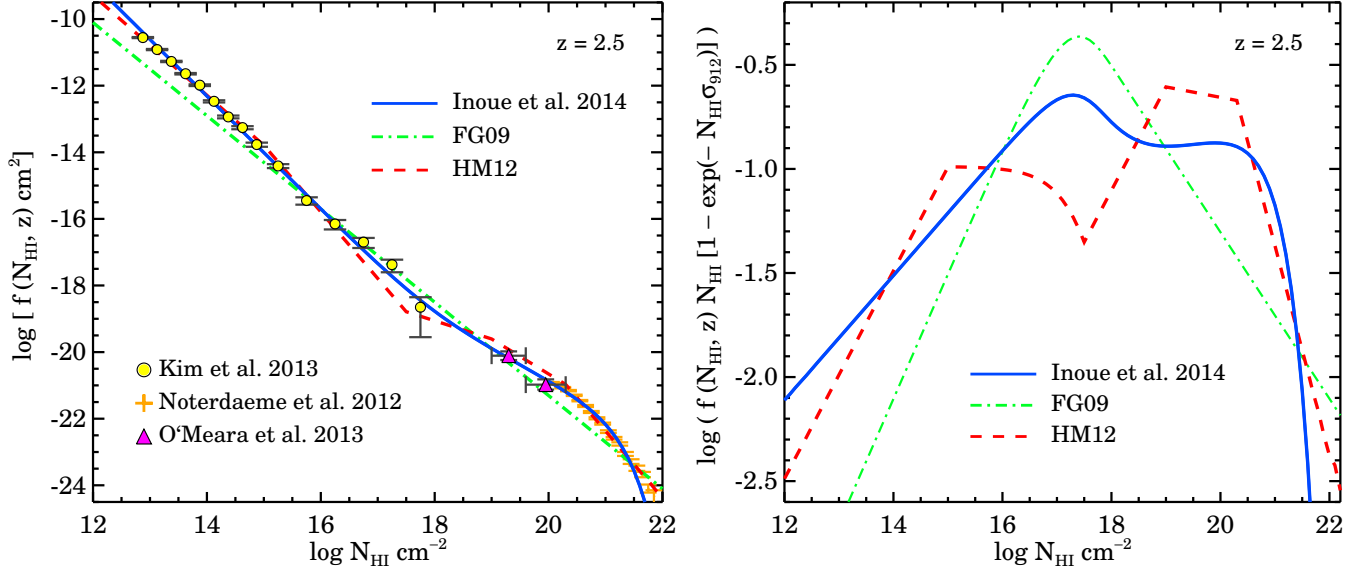


Figure 8. *Left-hand panel:* The $f(N_{\text{HI}}, z)$ at $z = 2.5$ from observations at different N_{HI} (Kim et al. 2013; Noterdaeme et al. 2012; O'Meara et al. 2013) and the fits used by HM12 and FG09 along with the updated fits given in Inoue et al. (2014). *Right-hand panel:* A quantity $N_{\text{HI}} f(N_{\text{HI}}, z) [1 - \exp(-N_{\text{HI}} \sigma_0)]$ that determines the contribution of N_{HI} to τ_{eff} . Mostly $\log N_{\text{HI}}(\text{cm}^{-2})$ range from 15 to 21 (and $\eta/4$ times small N_{HI}) dominates the τ_{eff} for H I (and He II) ionizing photons.

$f(N_{\text{HI}}, z)$ fits are shown in the right-hand panel of Fig. 8, where a contribution of τ_{eff} at each N_{HI} is represented by quantity $N_{\text{HI}} f(N_{\text{HI}}, z) [1 - \exp(-N_{\text{HI}} \sigma_{912})]$. When we use the $f(N_{\text{HI}}, z)$ from HM12 instead of Inoue et al. (2014), at $z < 3$ our $\Gamma_{\text{H I}}$ reduces by 10% (at $z \sim 2.5$ and by 25% at $z \sim 0.5$) to 40% (at $z \sim 0$) and $\Gamma_{\text{He II}}$ increases by similar amount (because of lower η due to small $\Gamma_{\text{H I}}$). These changes are smaller than or comparable to the current measurement uncertainties on $\Gamma_{\text{He II}}$ and $\Gamma_{\text{H I}}$ (see figure 16 of Gaikwad et al. 2017a). We also note that such a change in $f(N_{\text{HI}}, z)$ does not affect the spectral shape of the UVB significantly (see also Fig. 9 of HM12). However, note that, even if we use different $f(N_{\text{HI}}, z)$ that can change the UVB, the f_{esc} will be adjusted to get the same $\Gamma_{\text{H I}}$ measurements, which further reduces differences in $\Gamma_{\text{He II}}$ as well. The change in $\Gamma_{\text{H I}}$ and $\Gamma_{\text{He II}}$ is less than the change arising from varying the α by 0.2. Therefore, the uncertainties in $f(N_{\text{HI}}, z)$ have smaller impact on the UVB compared to the uncertainties in other parameters, especially the SED of type-1 QSOs.

The value of η calculated using equation (5) in optically thick He II regions depends on the assumption that the discrete absorbers in the IGM have line-of-sight thickness equal to the Jeans scale. Changing this thickness (by factors upto ~ 4) can affect the estimate of He II ionizing UVB due to change in η , however its impact on the UVB is quite small since it affects only small number of high column density absorbers.

4.4.4 Caveats from basic assumptions

Main caveats in the H I and He II ionizing part of the UVB is that the assumption of uniform and homogeneous UVB, which is not valid at all redshifts. It is certainly a reasonable assumption for H I ionizing UVB at $z < 5.5$ and He II ionizing UVB at $z < 2.5$ where respective reionization events

are believed to be completed. The equation 1 can provide reasonable estimates of UVB only in the regime where mean free path of (H I and He II) ionizing photons is large. Large fluctuations in the UVB are expected at redshifts where the respective reionizations are still in progress. At these redshifts, the homogeneous H I (He II) ionizing UVB calculated using equation 1 and its predictions for photoionization and photoheating rates can not capture the effects of large fluctuations in the radiation fields. As shown by Oñorbe et al. (2017a), these rates (from FG09 and HM12) will prematurely heat the IGM and reionize the H I and He II very early giving observationally inconsistent reionization histories and incorrect feedback on galaxy formation. Note that, even for our UVB models the consistency with reionization constraints shown in Section 4.4.2 (left and middle panel of Fig. 5), is just a sanity check on the ionizing emissivity used in UVB calculations and independent of the UVB estimates. Therefore at these redshifts, a large scatter expected in the photoheating and photoionization rates should be properly implemented in the cosmological hydrodynamic simulations. This can be achieved by modifying these rates as shown in Oñorbe et al. (2017a). Such a modification depends on how the physics of reionization is implemented in simulations, the assumed evolution of mean free path for ionizing photons and the SED of ionizing sources (Oñorbe et al. 2017a; Puchwein et al. 2018). Moreover, in absence of the observational constraints on the mean free paths and SEDs of ionizing sources at these redshifts, such a modification to the photoionization and photoheating rates can not be unique. Novel methods for determining accurate timing and heat-injection during reionization (e.g., Padmanabhan et al. 2014; Oñorbe et al. 2017b) will prove valuable in future to resolve these issues.

Even after completion of the reionization, significant fluctuations in the UVB are expected (e.g., Furlanetto & Mesinger 2009; Furlanetto 2009;

([Davies & Furlanetto 2016](#); [Davies et al. 2017](#)). In addition, the recently reionized gas may take some time to reach ionization and thermal equilibrium. Our calculations do not consider these non-equilibrium conditions (e.g., [Puchwein et al. 2015](#)). Also, most of the measurements of $\Gamma_{\text{H}\,\text{I}}$ that we used to constrain the ionizing emissivity from galaxies, are obtained from observed Lyman- α forest by modeling the IGM under the assumption of ionization and thermal equilibrium. A consolidated efforts are needed to get these issues sorted-out around the epoch of $\text{H}\,\text{i}$ and $\text{He}\,\text{II}$ reionization.

In the UVB calculations, several assumptions related to the input parameters are made in absence of the concrete observational constraints. For example, the QSO SED has been assumed to be the same at all redshifts in absence of significant observational evidence of its redshift evolution ([Stevans et al. 2014](#); [Tilton et al. 2016](#)). Also, it has been assumed that the type-1 QSO SED follows a single power-law for $\lambda < 912 \text{ \AA}$ upto wavelengths $\sim 50 \text{ \AA}$, although available observations only probe upto 425 \AA . Moreover, a single power-law may not be a good approximation to small wavelengths (e.g., [Tilton et al. 2016](#); [Khaire 2017](#)). Similarly for galaxies, although mild metallicity evolution does not affect intrinsic SEDs, the IMF and other stellar population parameters have been assumed to be the same at all redshifts. The obtained f_{esc} and SED of galaxies can be different for top heavy IMFs ([Topping & Shull 2015](#)) and including stellar rotation ([Ma et al. 2015](#)) and binary stars ([Rosdahl et al. 2018](#)) in the population synthesis models. For galaxies, a crucial assumption, as mentioned before, is the scaling of intrinsic galaxy SED by f_{esc} . Because of this our another assumption, a single dust extinction curve at all z , does not affect UVB but can change EBL at FIR wavelength due to the corresponding change in A_{FUV} and SFRD that preserves the emissivities till near-IR wavelengths (see [KS15b](#)).

In spite of all these uncertainties, we provide EBL models that are consistent with currently available observations at all redshifts and wavelengths. Better constraints on $\Gamma_{\text{H}\,\text{I}}$ at $0.5 \leq z \leq 2.0$ and at $z > 5$, well defined QLFs at low luminosity end and more measurements of τ_{HeII} at $z > 2$ will provide better constraints on the UVB models.

5 SUMMARY

The EBL is extensively used by the astronomical community for studying (i) spectral energy distribution of blazars in GeV energies, (ii) metal line absorption systems to derive density, metallicity and size of the absorbing gas and their redshift evolution and (iii) ionization and thermal state of the IGM over cosmic time. As the spectrum of EBL can not be directly measured at all epochs, it has to be modeled using the available observations of the source emissivities and IGM opacities with appropriate cosmological radiative transport. Thus it is important to have EBL computed time to time with latest parameters that govern the source emissivities and IGM opacities. In addition, it is important to quantify the allowed variations in computed EBL at each epoch so that one can estimate systemic uncertainties arising from EBL uncertainties while interpreting the data.

With these motivations, we present new synthesis models of the EBL which cover more than fifteen orders of mag-

nitude in wavelength from FIR to TeV γ -rays (see Fig. 6 for $z = 0$ EBL). Our main focus of this paper is on modeling the observationally consistent extreme-UV and soft X-ray background, which is essential for studying the metal absorption lines observed in QSO spectra.

In our EBL synthesis model, we use updated inputs such as SFRD and A_{FUV} for galaxies, QSO emissivity and $\text{H}\,\text{i}$ distribution of the IGM. We determine average escape fraction (f_{esc}) of $\text{H}\,\text{i}$ ionizing photons from galaxies which can reproduce the available recent measurements of the $\text{H}\,\text{i}$ photoionization rates at $z < 6.5$ (the left-hand panel of Fig. 3 and Fig. 4) and provide $\text{H}\,\text{i}$ reionization history consistent with many new measurements of $\text{H}\,\text{i}$ fraction at $z > 6$ and electron scattering optical depth to CMB (Fig. 5). The UV background at $z < 3$ is predominantly contributed by QSOs whereas galaxies contribute significantly to the $\text{H}\,\text{i}$ ionizing emissivity at $z > 3$ (see also [Khaire et al. 2016](#); [Gaikwad et al. 2017a](#)) as evident from a sharp increase in the required $f_{\text{esc}}(z)$ (see Fig. 3).

For our fiducial EBL model, we take type-1 QSO extreme UV SED as $f_{\nu} \propto \nu^{\alpha}$ with power-law slope $\alpha = -1.8$ from [Khaire \(2017\)](#), which consistently reproduce the $2.5 < z < 3.5$ measurements of Lyman- α effective optical depths, photoionization rates and reionization redshift of $\text{He}\,\text{II}$ (the right-hand panel of Fig. 4 and Fig. 5). Since available measurements of α show large variation, we also provide six other EBL models (in Appendix) calculated for different values of α from -1.4 to -2.0 consistent with recent measurements of α from [Shull et al. \(2012\)](#), [Stevans et al. \(2014\)](#) and [Lusso et al. \(2015\)](#). At X-ray and γ -ray energies, we modified the form of type-1 QSO SED and constructed a SED for type-2 QSOs (including γ -ray emitting blazars) following [Sazonov et al. \(2004\)](#) to consistently reproduce the measurements of local X-ray and γ -ray background (Fig. D3). We find that, EBL models constructed in this way with $\alpha > -1.5$ are not consistent with $\text{He}\,\text{II}$ Lyman- α effective optical depths (see also [Khaire 2017](#)) and some of the soft-X-ray background measurements.

Because the UV background is an important tool to study the time evolution in physical and chemical properties of the IGM and CGM, it needs to be consistent with various observational constraints. We discuss in details the uncertainties and caveats arising from several assumptions in the modeling of UV background (see Section 4.4). We are working on addressing some of the caveats such as non-equilibrium ionization and thermal evolution of the IGM and its impact on the UV background around the epochs of $\text{H}\,\text{i}$ and $\text{He}\,\text{II}$ reionization. Within the framework discussed here and in the previous UV background models, a major uncertainty lies in the spectral shape, therefore improved observational constraints on the QSO SEDs and escaping Lyman-continuum SEDs of galaxies are important. Also, new techniques to constrain spectral shape of the UV background by using metal absorption lines are required (e.g., [Fechner 2011](#); [Finlator et al. 2016](#)). Our UV background models obtained for different QSO SEDs will be useful for such studies.

For public use we provide the EBL tables, the photoionization and photoheating rates of $\text{H}\,\text{i}$, $\text{He}\,\text{i}$ and $\text{He}\,\text{II}$ ob-

tained from EBL models, and γ -ray effective optical depths at all redshifts.⁵

ACKNOWLEDGEMENT

We thank Marco Ajello, Nico Cappelluti and Eugene Churazov for providing the X-ray background data. We thank Prakash Gaikwad, Tirthankar Roy Choudhury, Aseem Paranjape and Kandaswamy Subramanian for helpful discussions throughout the development of this project. VK thanks Fred Davies, Jose Onorbe, Tobias Schmidt and other ENIGMA group members at UCSB for valuable comments on the manuscript.

REFERENCES

Ackermann M., et al., 2012, *Science*, **338**, 1190
 Ackermann M., et al., 2015, *ApJ*, **799**, 86
 Adams J. J., Uson J. M., Hill G. J., MacQueen P. J., 2011, *ApJ*, **728**, 107
 Ajello M., et al., 2008, *ApJ*, **689**, 666
 Ajello M., et al., 2015, *ApJ*, **800**, L27
 Andrews S. K., et al., 2017, *MNRAS*, **470**, 1342
 Antonucci R., 1993, *ARA&A*, **31**, 473
 Aracil B., Petitjean P., Pichon C., Bergeron J., 2004, *A&A*, **419**, 811
 Arlen T. C., Vassiliev V. V., Weisgarber T., Wakely S. P., Yusef Shafi S., 2012, preprint, ([arXiv:1210.2802](https://arxiv.org/abs/1210.2802))
 Bañados E., et al., 2017, preprint, ([arXiv:1712.01860](https://arxiv.org/abs/1712.01860))
 Bajtlik S., Duncan R. C., Ostriker J. P., 1988, *ApJ*, **327**, 570
 Ballantyne D. R., Draper A. R., Madsen K. K., Rigby J. R., Treister E., 2011, *ApJ*, **736**, 56
 Becker G. D., Bolton J. S., 2013, *MNRAS*, **436**, 1023
 Becker R. H., et al., 2001, *AJ*, **122**, 2850
 Becker G. D., Rauch M., Sargent W. L. W., 2007, *ApJ*, **662**, 72
 Becker G. D., Bolton J. S., Haehnelt M. G., Sargent W. L. W., 2011, *MNRAS*, **410**, 1096
 Becker G. D., Hewett P. C., Worseck G., Prochaska J. X., 2013, *MNRAS*, **430**, 2067
 Behroozi P. S., Wechsler R. H., Conroy C., 2013, *ApJ*, **770**, 57
 Bergeron J., Aracil B., Petitjean P., Pichon C., 2002, *A&A*, **396**, L11
 Bergvall N., Zackrisson E., Andersson B.-G., Arnberg D., Masegosa J., Östlin G., 2006, *A&A*, **448**, 513
 Bolton J. S., Haehnelt M. G., 2007, *MNRAS*, **382**, 325
 Borthakur S., Heckman T. M., Leitherer C., Overzier R. A., 2014, *Science*, **346**, 216
 Bouwens R. J., et al., 2012, *ApJ*, **754**, 83
 Bouwens R. J., et al., 2015, *ApJ*, **803**, 34
 Bridge C. R., et al., 2010, *ApJ*, **720**, 465
 Buchner J., et al., 2015, *ApJ*, **802**, 89
 Burgarella D., et al., 2013, *A&A*, **554**, A70
 Calverley A. P., Becker G. D., Haehnelt M. G., Bolton J. S., 2011, *MNRAS*, **412**, 2543
 Cappelluti N., et al., 2017, *ApJ*, **837**, 19
 Choudhury T. R., Puchwein E., Haehnelt M. G., Bolton J. S., 2015, *MNRAS*, **452**, 261
 Churazov E., et al., 2007, *A&A*, **467**, 529
 Comastri A., Setti G., Zamorani G., Hasinger G., 1995, *A&A*, **296**, 1
 Compostella M., Cantalupo S., Porciani C., 2013, *MNRAS*, **435**, 3169
 Conroy C., Kratter K. M., 2012, *ApJ*, **755**, 123
 Cowie L. L., Barger A. J., Trouille L., 2009, *ApJ*, **692**, 1476
 Croom S. M., et al., 2009, *MNRAS*, **399**, 1755
 D’Aloisio A., McQuinn M., Davies F. B., Furlanetto S. R., 2018, *MNRAS*, **473**, 560
 D’Odorico V., et al., 2013, *MNRAS*, **435**, 1198
 Dall’Aglio A., Wisotzki L., Worseck G., 2008, *A&A*, **491**, 465
 Danforth C. W., Shull J. M., 2005, *ApJ*, **624**, 555
 Davé R., Hernquist L., Katz N., Weinberg D. H., 1999, *ApJ*, **511**, 521
 Davies F. B., Furlanetto S. R., 2016, *MNRAS*, **460**, 1328
 Davies F. B., Furlanetto S. R., Dixon K. L., 2017, *MNRAS*, **465**, 2886
 Dayal P., Ferrara A., Saro A., 2010, *MNRAS*, **402**, 1449
 Dijkstra M., 2017, preprint, ([arXiv:1704.03416](https://arxiv.org/abs/1704.03416))
 Dijkstra M., Haiman Z., Spaans M., 2006, *ApJ*, **649**, 14
 Dole H., et al., 2006, *A&A*, **451**, 417
 Domínguez A., et al., 2011, *MNRAS*, **410**, 2556
 Dove J. B., Shull J. M., 1994, *ApJ*, **423**, 196
 Draper A. R., Ballantyne D. R., 2009, *ApJ*, **707**, 778
 Driver S. P., et al., 2016a, *MNRAS*, **455**, 3911
 Driver S. P., et al., 2016b, *ApJ*, **827**, 108
 Dwek E., Arendt R. G., 1998, *ApJ*, **508**, L9
 Dwek E., Krennrich F., 2013, *Astroparticle Physics*, **43**, 112
 Efstathiou G., 1992, *MNRAS*, **256**, 43P
 Fan X., et al., 2006, *AJ*, **132**, 117
 Fardal M. A., Giroux M. L., Shull J. M., 1998, *AJ*, **115**, 2206
 Faucher-Giguère C.-A., Prochaska J. X., Lidz A., Hernquist L., Zaldarriaga M., 2008, *ApJ*, **681**, 831
 Faucher-Giguère C.-A., Lidz A., Zaldarriaga M., Hernquist L., 2009, *ApJ*, **703**, 1416
 Fechner C., 2011, *A&A*, **532**, A62
 Fechner C., et al., 2006, *A&A*, **455**, 91
 Ferland G. J., et al., 2013, *Rev. Mex. Astron. Astrofis.*, **49**, 137
 Ferrara A., Scannapieco E., Bergeron J., 2005, *ApJ*, **634**, L37
 Finke J. D., Razzaque S., Dermer C. D., 2010, *ApJ*, **712**, 238
 Finke J. D., Reyes L. C., Georganopoulos M., Reynolds K., Ajello M., Fegan S. J., McCann K., 2015, *ApJ*, **814**, 20
 Finlator K., Oh S. P., Özel F., Davé R., 2012, *MNRAS*, **427**, 2464
 Finlator K., Oppenheimer B. D., Davé R., Zackrisson E., Thompson R., Huang S., 2016, *MNRAS*, **459**, 2299
 Franceschini A., Rodighiero G., Vaccari M., 2008, *A&A*, **487**, 837
 Fujita A., Martin C. L., Mac Low M.-M., Abel T., 2003, *ApJ*, **599**, 50
 Fukada Y., Hayakawa S., Kasahara I., Makino F., Tanaka Y., Sreekanth B. V., 1975, *Nature*, **254**, 398
 Fumagalli M., O’Meara J. M., Prochaska J. X., Worseck G., 2013, *ApJ*, **775**, 78
 Fumagalli M., Haardt F., Theuns T., Morris S. L., Cantalupo S., Madau P., Fossati M., 2017, *MNRAS*, **467**, 4802
 Furlanetto S. R., 2009, *ApJ*, **703**, 702
 Furlanetto S. R., Mesinger A., 2009, *MNRAS*, **394**, 1667
 Gaikwad P., Khaire V., Choudhury T. R., Srianand R., 2017a, *MNRAS*, **466**, 838
 Gaikwad P., Srianand R., Choudhury T. R., Khaire V., 2017b, *MNRAS*, **467**, 3172
 Gaikwad P., Choudhury T. R., Srianand R., Khaire V., 2018, *MNRAS*, **474**, 2233
 Gendreau K. C., et al., 1995, *PASJ*, **47**, L5
 Georgakakis A., et al., 2017, *MNRAS*, **469**, 3232
 Giallongo E., et al., 2015, *A&A*, **578**, A83
 Gilli R., Comastri A., Hasinger G., 2007, *A&A*, **463**, 79
 Gilmore R. C., Somerville R. S., Primack J. R., Domínguez A., 2012, *MNRAS*, **422**, 3189
 Giroux M. L., Shapiro P. R., 1996, *ApJS*, **102**, 191

⁵ All tables are available at <ftp://ftp.iucaa.in/in.coming/KS18EBL/> and <http://vikramkhaire.weebly.com/downloads.html>

Glikman E., Djorgovski S. G., Stern D., Dey A., Jannuzi B. T., Lee K.-S., 2011, *ApJ*, **728**, L26

Gnedin N. Y., Hui L., 1998, *MNRAS*, **296**, 44

Gnedin N. Y., Kravtsov A. V., Chen H.-W., 2008, *ApJ*, **672**, 765

Gohil R., Ballantyne D. R., 2017, preprint, ([arXiv:1711.05268](https://arxiv.org/abs/1711.05268))

Gordon K. D., Clayton G. C., Misselt K. A., Landolt A. U., Wolff M. J., 2003, *ApJ*, **594**, 279

Goto T., Utsumi Y., Hattori T., Miyazaki S., Yamauchi C., 2011, *MNRAS*, **415**, L1

Gould R. J., Schréder G., 1966, *Physical Review Letters*, **16**, 252

Grazian A., et al., 2017, *A&A*, **602**, A18

Greig B., Mesinger A., 2017, *MNRAS*, **465**, 4838

Greig B., Mesinger A., Haiman Z., Simcoe R. A., 2017, *MNRAS*, **466**, 4239

Gronke M., Dijkstra M., McCourt M., Oh S. P., 2016, *ApJ*, **833**, L26

Gruber D. E., Matteson J. L., Peterson L. E., Jung G. V., 1999, *ApJ*, **520**, 124

Guaita L., et al., 2016, *A&A*, **587**, A133

Gunn J. E., Peterson B. A., 1965, *ApJ*, **142**, 1633

Gurvich A., Burkhardt B., Bird S., 2017, *ApJ*, **835**, 175

Haardt F., Madau P., 1996, *ApJ*, **461**, 20

Haardt F., Madau P., 2001, in Neumann D. M., Tran J. T. V., eds, Clusters of Galaxies and the High Redshift Universe Observed in X-rays. ([arXiv:astro-ph/0106018](https://arxiv.org/abs/astro-ph/0106018))

Haardt F., Madau P., 2012, *ApJ*, **746**, 125

Helgason K., Kashlinsky A., 2012, *ApJ*, **758**, L13

Hernquist L., Katz N., Weinberg D. H., Miralda-Escudé J., 1996, *ApJ*, **457**, L51

Hiss H., Walther M., Hennawi J. F., Oñorbe J., O'Meara J. M., Rorai A., 2017, preprint, ([arXiv:1710.00700](https://arxiv.org/abs/1710.00700))

Hopkins P. F., Richards G. T., Hernquist L., 2007, *ApJ*, **654**, 731

Hui L., Gnedin N. Y., 1997, *MNRAS*, **292**, 27

Hussain T., Muzahid S., Srianand A., Srianand R., Wakker B. P., Charlton J. C., Pathak A., 2015, *MNRAS*, **446**, 2444

Hussain T., Khaire V., Srianand R., Muzahid S., Pathak A., 2017, *MNRAS*, **466**, 3133

Inoue Y., Inoue S., Kobayashi M. A. R., Makiya R., Niino Y., Totani T., 2013, *ApJ*, **768**, 197

Inoue A. K., Shimizu I., Iwata I., Tanaka M., 2014, *MNRAS*, **442**, 1805

Inoue A. K., et al., 2018, preprint, ([arXiv:1801.00067](https://arxiv.org/abs/1801.00067))

Izotov Y. I., Schaerer D., Thuan T. X., Worseck G., Guseva N. G., Orlitová I., Verhamme A., 2016a, *MNRAS*, **461**, 3683

Izotov Y. I., Orlitová I., Schaerer D., Thuan T. X., Verhamme A., Guseva N. G., Worseck G., 2016b, *Nature*, **529**, 178

Izotov Y. I., Schaerer D., Worseck G., Guseva N. G., Thuan T. X., Verhamme A., Orlitová I., Fricke K. J., 2018, *MNRAS*, **474**, 4514

Janknecht E., Reimers D., Lopez S., Tytler D., 2006, *A&A*, **458**, 427

Japelj J., et al., 2017, *MNRAS*, **468**, 389

Kashikawa N., et al., 2015, *ApJ*, **798**, 28

Khaire V., 2017, *MNRAS*, **471**, 255

Khaire V., Srianand R., 2013, *MNRAS*, **431**, L53

Khaire V., Srianand R., 2015a, *MNRAS*, **451**, L30

Khaire V., Srianand R., 2015b, *ApJ*, **805**, 33

Khaire V., Srianand R., Choudhury T. R., Gaikwad P., 2016, *MNRAS*, **457**, 4051

Kim T.-S., Cristiani S., D'Odorico S., 2001, *A&A*, **373**, 757

Kim T.-S., Partl A. M., Carswell R. F., Müller V., 2013, *A&A*, **552**, A77

Kinzer R. L., Jung G. V., Gruber D. E., Matteson J. L., Peterson L. E., 1997, *ApJ*, **475**, 361

Kirkman D., Tytler D., Lubin D., Charlton J., 2007, *MNRAS*, **376**, 1227

Kneiske T. M., Dole H., 2010, *A&A*, **515**, A19

Kollmeier J. A., et al., 2014, *ApJ*, **789**, L32

Kriss G. A., et al., 2001, *Science*, **293**, 1112

Kulkarni V. P., Fall S. M., 1993, *ApJ*, **413**, L63

Kulkarni G., Hennawi J. F., Oñorbe J., Rorai A., Springel V., 2015, *ApJ*, **812**, 30

La Plante P., Trac H., 2016, *ApJ*, **828**, 90

Larson D., et al., 2011, *ApJS*, **192**, 16

Lehner N., O'Meara J. M., Fox A. J., Howk J. C., Prochaska J. X., Burns V., Armstrong A. A., 2014, *ApJ*, **788**, 119

Leitet E., Bergvall N., Hayes M., Linné S., Zackrisson E., 2013, *A&A*, **553**, A106

Leitherer C., et al., 1999, *ApJS*, **123**, 3

Leitherer C., Hernandez S., Lee J. C., Oey M. S., 2016, *ApJ*, **823**, 64

Lidz A., Faucher-Giguère C.-A., Dall'Aglio A., McQuinn M., Fechner C., Zaldarriaga M., Hernquist L., Dutta S., 2010, *ApJ*, **718**, 199

Liu T., et al., 2017, *ApJS*, **232**, 8

Lusso E., et al., 2013, *ApJ*, **777**, 86

Lusso E., Worseck G., Hennawi J. F., Prochaska J. X., Vignali C., Stern J., O'Meara J. M., 2015, *MNRAS*, **449**, 4204

Ma X., Kasen D., Hopkins P. F., Faucher-Giguère C.-A., Quataert E., Kereš D., Murray N., 2015, *MNRAS*, **453**, 960

Madau P., Dickinson M., 2014, *ARA&A*, **52**, 415

Madau P., Haardt F., 2015, *ApJ*, **813**, L8

Madau P., Haardt F., Rees M. J., 1999, *ApJ*, **514**, 648

Marchi F., et al., 2017, *A&A*, **601**, A73

Mason C. A., Treu T., Dijkstra M., Mesinger A., Trenti M., Pentericci L., de Barros S., Vanzella E., 2017, preprint, ([arXiv:1709.05356](https://arxiv.org/abs/1709.05356))

Masters D., et al., 2012, *ApJ*, **755**, 169

Matthee J., Sobral D., Best P., Khostovan A. A., Oteo I., Bouwens R., Röttgering H., 2017, *MNRAS*, **465**, 3637

McGreer I. D., et al., 2013, *ApJ*, **768**, 105

McGreer I. D., Mesinger A., D'Odorico V., 2015, *MNRAS*, **447**, 499

McGreer I. D., Fan X., Jiang L., Cai Z., 2017, preprint, ([arXiv:1710.09390](https://arxiv.org/abs/1710.09390))

McLeod D. J., McLure R. J., Dunlop J. S., Robertson B. E., Ellis R. S., Targett T. A., 2015, *MNRAS*, **450**, 3032

McQuinn M., 2016, *ARA&A*, **54**, 313

McQuinn M., Worseck G., 2014, *MNRAS*, **440**, 2406

McQuinn M., Lidz A., Zaldarriaga M., Hernquist L., Hopkins P. F., Dutta S., Faucher-Giguère C.-A., 2009, *ApJ*, **694**, 842

Meiksin A. A., 2009, *Reviews of Modern Physics*, **81**, 1405

Meiring J. D., Tripp T. M., Werk J. K., Howk J. C., Jenkins E. B., Prochaska J. X., Lehner N., Sembach K. R., 2013, *ApJ*, **767**, 49

Mesinger A., Aykutalp A., Vanzella E., Pentericci L., Ferrara A., Dijkstra M., 2015, *MNRAS*, **446**, 566

Micheva G., Iwata I., Inoue A. K., Matsuda Y., Yamada T., Hayashino T., 2017, *MNRAS*, **465**, 316

Miralda-Escudé J., Ostriker J. P., 1990, *ApJ*, **350**, 1

Mostardi R. E., Shapley A. E., Steidel C. C., Trainor R. F., Reddy N. A., Siana B., 2015, *ApJ*, **810**, 107

Muzahid S., Srianand R., Petitjean P., 2011, *MNRAS*, **410**, 2193

Muzahid S., Srianand R., Bergeron J., Petitjean P., 2012, *MNRAS*, **421**, 446

Muzahid S., Fonseca G., Roberts A., Rosenwasser B., Richter P., Narayanan A., Churchill C., Charlton J., 2017, preprint, ([arXiv:1709.03999](https://arxiv.org/abs/1709.03999))

Narayanan A., Savage B. D., Wakker B. P., 2012, *ApJ*, **752**, 65

Narayanan A., Savage B. D., Mishra P. K., Wakker B. P., Khaire V., Wadadekar Y., 2018, *MNRAS*, **476**, 232

Neronov A., Vovk I., 2010, *Science*, **328**, 73

Neufeld D. A., 1990, *ApJ*, **350**, 216

Neufeld D. A., 1991, *ApJ*, **370**, L85

Noterdaeme P., Ledoux C., Srianand R., Petitjean P., Lopez S., 2009, *A&A*, **503**, 765

Noterdaeme P., et al., 2012, *A&A*, **547**, L1

Oñorbe J., Hennawi J. F., Lukić Z., 2017a, *ApJ*, **837**, 106

Oñorbe J., Hennawi J. F., Lukić Z., Walther M., 2017b, *ApJ*, **847**, 63

O'Meara J. M., Prochaska J. X., Burles S., Prochster G., Bernstein R. A., Burgess K. M., 2007, *ApJ*, **656**, 666

O'Meara J. M., Prochaska J. X., Worseck G., Chen H.-W., Madau P., 2013, *ApJ*, **765**, 137

Oesch P. A., et al., 2014, *ApJ*, **786**, 108

Paardekooper J.-P., Pelupessy F. I., Altay G., Kruip C. J. H., 2011, *A&A*, **530**, A87

Pachat S., Narayanan A., Muzahid S., Khaire V., Srianand R., Wakker B. P., Savage B. D., 2016, *MNRAS*, **458**, 733

Pachat S., Narayanan A., Khaire V., Savage B. D., Muzahid S., Wakker B. P., 2017, *MNRAS*, **471**, 792

Padmanabhan T., 2002, Theoretical Astrophysics - Volume 3, Galaxies and Cosmology, [doi:10.2277/0521562422](https://doi.org/10.2277/0521562422).

Padmanabhan H., Choudhury T. R., Srianand R., 2014, *MNRAS*, **443**, 3761

Palanque-Delabrouille N., et al., 2013, *A&A*, **551**, A29

Paresce F., McKee C. F., Bowyer S., 1980, *ApJ*, **240**, 387

Peebles P. J. E., 1993, Principles of Physical Cosmology

Peeples M. S., Werk J. K., Tumlinson J., Oppenheimer B. D., Prochaska J. X., Katz N., Weinberg D. H., 2014, *ApJ*, **786**, 54

Péroux C., Dessauges-Zavadsky M., D'Odorico S., Sun Kim T., McMahon R. G., 2005, *MNRAS*, **363**, 479

Planck Collaboration et al., 2016a, *A&A*, **594**, A13

Planck Collaboration et al., 2016b, *A&A*, **596**, A107

Prochaska J. X., Worseck G., O'Meara J. M., 2009, *ApJ*, **705**, L113

Prochaska J. X., O'Meara J. M., Worseck G., 2010, *ApJ*, **718**, 392

Prochaska J. X., Madau P., O'Meara J. M., Fumagalli M., 2014, *MNRAS*, **438**, 476

Prochaska J. X., et al., 2017, *ApJ*, **837**, 169

Puchwein E., Bolton J. S., Haehnelt M. G., Madau P., Becker G. D., Haardt F., 2015, *MNRAS*, **450**, 4081

Puchwein E., Haardt F., Haehnelt M. G., Madau P., 2018, preprint, ([arXiv:1801.04931](https://arxiv.org/abs/1801.04931))

Rao S. M., Turnshek D. A., Nestor D. B., 2006, *ApJ*, **636**, 610

Rauch M., et al., 1997, *ApJ*, **489**, 7

Revnivtsev M., Gilfanov M., Sunyaev R., Jahoda K., Markwardt C., 2003, *A&A*, **411**, 329

Ricci F., Marchesi S., Shankar F., La Franca F., Civano F., 2017, *MNRAS*, **465**, 1915

Rieke G. H., Alonso-Herrero A., Weiner B. J., Pérez-González P. G., Blaylock M., Donley J. L., Marcillac D., 2009, *ApJ*, **692**, 556

Rorai A., et al., 2017, *Science*, **356**, 418

Rosdahl J., et al., 2018, preprint, ([arXiv:1801.07259](https://arxiv.org/abs/1801.07259))

Ross N. P., et al., 2013, *ApJ*, **773**, 14

Rutkowski M. J., et al., 2016, *ApJ*, **819**, 81

Rutkowski M. J., et al., 2017, *ApJ*, **841**, L27

Salpeter E. E., 1955, *ApJ*, **121**, 161

Samui S., Srianand R., Subramanian K., 2007, *MNRAS*, **377**, 285

Savage B. D., Lehner N., Wakker B. P., Sembach K. R., Tripp T. M., 2005, *ApJ*, **626**, 776

Savage B. D., Narayanan A., Lehner N., Wakker B. P., 2011, *ApJ*, **731**, 14

Savage B. D., Kim T.-S., Wakker B. P., Keeney B., Shull J. M., Stocke J. T., Green J. C., 2014, *ApJS*, **212**, 8

Sazonov S. Y., Ostriker J. P., Sunyaev R. A., 2004, *MNRAS*, **347**, 144

Schaye J., 2001, *ApJ*, **559**, 507

Schaye J., Aguirre A., Kim T.-S., Theuns T., Rauch M., Sargent W. L. W., 2003, *ApJ*, **596**, 768

Schenker M. A., Ellis R. S., Konidaris N. P., Stark D. P., 2014, *ApJ*, **795**, 20

Schulze A., Wisotzki L., Husemann B., 2009, *A&A*, **507**, 781

Scott J. E., Kriss G. A., Brotherton M., Green R. F., Hutchings J., Shull J. M., Zheng W., 2004, *ApJ*, **615**, 135

Scully S. T., Malkan M. A., Stecker F. W., 2014, *ApJ*, **784**, 138

Shapiro P. R., Giroux M. L., Babul A., 1994, *ApJ*, **427**, 25

Shapley A. E., Steidel C. C., Strom A. L., Bogosavljević M., Reddy N. A., Siana B., Mostardi R. E., Rudie G. C., 2016, *ApJ*, **826**, L24

Shull J. M., Roberts D., Giroux M. L., Penton S. V., Fardal M. A., 1999, *AJ*, **118**, 1450

Shull J. M., Tumlinson J., Giroux M. L., Kriss G. A., Reimers D., 2004, *ApJ*, **600**, 570

Shull J. M., France K., Danforth C. W., Smith B., Tumlinson J., 2010, *ApJ*, **722**, 1312

Shull J. M., Harness A., Trenti M., Smith B. D., 2012, *ApJ*, **747**, 100

Shull J. M., Danforth C. W., Tilton E. M., 2014, *ApJ*, **796**, 49

Shull J. M., Moloney J., Danforth C. W., Tilton E. M., 2015, *ApJ*, **811**, 3

Siana B., et al., 2010, *ApJ*, **723**, 241

Siana B., et al., 2015, *ApJ*, **804**, 17

Smith B. M., et al., 2016, preprint, ([arXiv:1602.01555](https://arxiv.org/abs/1602.01555))

Songaila A., Cowie L. L., 1996, *AJ*, **112**, 335

Songaila A., Cowie L. L., 2010, *ApJ*, **721**, 1448

Springel V., Yoshida N., White S. D. M., 2001, *New Astron.*, **6**, 79

Srianand R., Khare P., 1996, *MNRAS*, **280**, 767

Stecker F. W., de Jager O. C., Salamon M. H., 1992, *ApJ*, **390**, L49

Stecker F. W., Baring M. G., Summerlin E. J., 2007, *ApJ*, **667**, L29

Stevans M. L., Shull J. M., Danforth C. W., Tilton E. M., 2014, *ApJ*, **794**, 75

Strong A. W., Moskalenko I. V., Reimer O., 2003, International Cosmic Ray Conference, **5**, 2687

Sunyaev R. A., 1969, *Astrophys. Lett.*, **3**, 33

Takeuchi T. T., Buat V., Burgarella D., 2005, *A&A*, **440**, L17

Tavecchio F., Ghisellini G., Bonnoli G., Foschini L., 2011, *MNRAS*, **414**, 3566

Telfer R. C., Zheng W., Kriss G. A., Davidsen A. F., 2002, *ApJ*, **565**, 773

Tilton E. M., Stevans M. L., Shull J. M., Danforth C. W., 2016, *ApJ*, **817**, 56

Topping M. W., Shull J. M., 2015, *ApJ*, **800**, 97

Treister E., Urry C. M., 2005, *ApJ*, **630**, 115

Treister E., Urry C. M., 2006, *ApJ*, **652**, L79

Treister E., Urry C. M., Virani S., 2009, *ApJ*, **696**, 110

Tripp T. M., Sembach K. R., Bowen D. V., Savage B. D., Jenkins E. B., Lehner N., Richter P., 2008, *ApJS*, **177**, 39

Upton Sanderbeck P. R., McQuinn M., D'Aloisio A., Werk J. K., 2017, preprint, ([arXiv:1710.07295](https://arxiv.org/abs/1710.07295))

Urry C. M., Padovani P., 1995, *PASP*, **107**, 803

Vanzella E., Siana B., Cristiani S., Nonino M., 2010, *MNRAS*, **404**, 1672

Vanzella E., et al., 2016, *ApJ*, **825**, 41

Viel M., Haehnelt M. G., Bolton J. S., Kim T.-S., Puchwein E., Nasir F., Wakker B. P., 2017, *MNRAS*, **467**, L86

Vito F., et al., 2017, preprint, ([arXiv:1709.07892](https://arxiv.org/abs/1709.07892))

Warwick R. S., Roberts T. P., 1998, *Astronomische Nachrichten*, **319**, 59

Watanabe K., Hartmann D. H., Leising M. D., The L.-S., Share G. H., Kinzer R. L., 1997, in Dermer C. D., Strickman M. S., Kurfess J. D., eds, American Institute of Physics Conference Series Vol. 410, Proceedings of the Fourth Compton Symposium. pp 1223–1227, [doi:10.1063/1.53933](https://doi.org/10.1063/1.53933)

Weidenspointner G., et al., 2000, in McConnell M. L., Ryan J. M., eds, American Institute of Physics Conference Series Vol. 510, American Institute of Physics Conference Series. pp 467–470, [doi:10.1063/1.1307028](https://doi.org/10.1063/1.1307028)

Weigel A. K., Schawinski K., Treister E., Urry C. M., Koss M., Trakhtenbrot B., 2015, *MNRAS*, **448**, 3167
 Weinberg D. H., Hernquist L., Katz N., 1997, *ApJ*, **477**, 8
 Weymann R. J., et al., 1998, *ApJ*, **506**, 1
 Worseck G., et al., 2011, *ApJ*, **733**, L24
 Worseck G., et al., 2014, *MNRAS*, **445**, 1745
 Worseck G., Prochaska J. X., Hennawi J. F., McQuinn M., 2016, *ApJ*, **825**, 144
 Wyithe J. S. B., Bolton J. S., 2011, *MNRAS*, **412**, 1926
 Zavala J., Vogelsberger M., Slatyer T. R., Loeb A., Springel V., 2011, *Phys. Rev. D*, **83**, 123513
 Zheng W., Kriss G. A., Telfer R. C., Grimes J. P., Davidsen A. F., 1997, *ApJ*, **475**, 469
 Zheng W., et al., 2004, *ApJ*, **605**, 631
 de Barros S., et al., 2016, *A&A*, **585**, A51

APPENDIX A: ESCAPE FRACTION MEASUREMENTS

In Table A1, we provide the details of the average escape fraction measurements which are shown in the left-hand panel of the Fig. 3. The f_{esc} is obtained using following relation

$$f_{\text{esc}} = f_{\text{esc}}^{\text{rel}} 10^{-0.4A_{\text{FUV}}} \left(\frac{f_{\lambda_{\text{FUV}}}}{f_{\lambda_i}} \right)_{\text{KS15}} \left(\frac{f_{\lambda_{\text{FUV}}}}{f_{\lambda_i}} \right)^{-1} \quad (\text{A1})$$

where, $f_{\text{esc}}^{\text{rel}}$ is the relative escape fraction provided in the respective references assuming an intrinsic value of $(f_{\lambda_{\text{FUV}}}/f_{\lambda_i})$ where λ_{FUV} denotes the rest wavelength at FUV and the λ_i denotes rest wavelength where ionizing photons have been observed. The $(f_{\lambda_{\text{FUV}}}/f_{\lambda_i})_{\text{KS15}}$ denotes the intrinsic value of $(f_{\lambda_{\text{FUV}}}/f_{\lambda_i})$ and $10^{-0.4A_{\text{FUV}}}$ is the dust correction from our fiducial galaxy emissivity model. We use the $1-\sigma$ value of f_{esc} given in Matthee et al. (2017) without any correction since they use an indirect method to obtain f_{esc} from H α emission.

APPENDIX B: γ -RAY OPACITY

The optical depth encountered by γ -rays depends on the energy of the gamma-rays, their source redshift z_0 and the number density of the EBL photons at each $z \leq z_0$. If $n(E_{\text{ebl}}, z)$ is the number density of the EBL photons at redshift z having energy E_{ebl} per unit energy then the optical depth encountered by γ -rays emitted at redshift z_0 with frequency $\nu_{\gamma}(1+z_0)$ and observed on Earth at frequency ν_{γ} is given by

$$\begin{aligned} \tau_{\gamma}(\nu_{\gamma}, z_0) &= \frac{1}{2} \int_0^{z_0} dz \frac{dl}{dz} \int_{-1}^1 d(\cos \theta) (1 - \cos \theta) \\ &\times \int_{E_{\text{min}}}^{\infty} dE_{\text{ebl}} n(E_{\text{ebl}}, z) \sigma(E_{\gamma}(1+z), E_{\text{ebl}}, \theta). \end{aligned} \quad (\text{B1})$$

Here $E_{\gamma} = h\nu_{\gamma}$,

$$E_{\text{min}} = \frac{2m_e^2 c^4}{h\nu_{\gamma}(1+z)(1-\cos \theta)}, \quad (\text{B2})$$

and $\sigma(E_{\gamma}(1+z), E_{\text{ebl}}, \theta)$ is the cross-section for pair production (see equation 14 of KS15b).

Using above equation, we calculate the $\tau_{\gamma}(\nu_{\gamma}, z)$ at different z for our fiducial EBL model (Q18) and EBL model with $\alpha = -1.4$. Note that to estimate τ_{γ} we include CMB

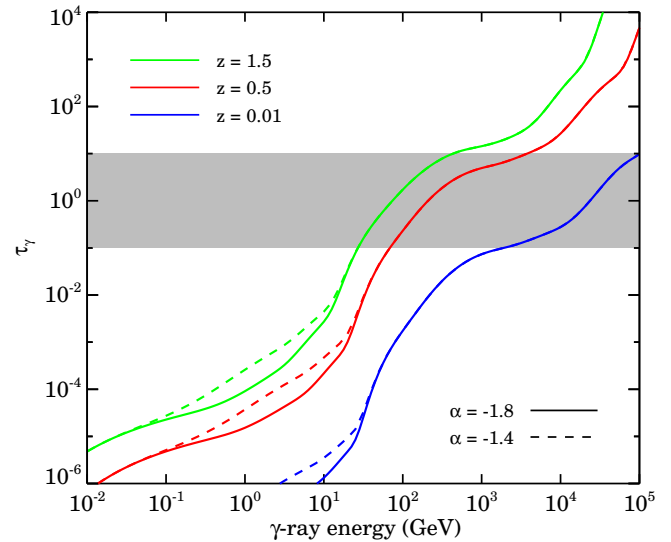


Figure B1. Optical depth (τ_{γ}) encountered by γ -rays for different energy (in GeV) observed on Earth which were emitted from redshift $z = 0.01$ (blue curves), $z = 0.5$ (red curves) and $z = 1.5$ (green curves). Solid and dashed curves are for our EBL models with $\alpha = -1.8$ (fiducial) and $\alpha = -1.4$. τ_{γ} is calculated by including CMB in both EBL models. Shaded region shows observationally relevant τ_{γ} values from 0.1 to 10 which are insensitive to the EBL photons with energy $E < 10$ eV and thus on values of assumed α .

in our EBL models. Results for three redshifts are shown in Fig. B1. The different features seen in the $\tau_{\gamma}(\nu_{\gamma})$ can be naively mapped to the features seen in the EBL. For example, the γ -rays with $E_{\gamma} < 20/(1+z)$ GeV (0.1/(1+z) GeV) are attenuated by EBL with $E_{\text{ebl}} > 13.6$ eV (500 eV), the γ -rays with $E_{\gamma} > 100/(1+z)$ TeV are affected by CMB, and the bump in τ_{γ} around 100 GeV is due to rest of the EBL. The shaded region in Fig. B1 shows the observationally relevant opacities from 0.1 to 10. Within this region, EBL models with different α give same τ_{γ} since it is dominated by low-energy photons ($E_{\text{ebl}} < 10$ eV) which do not depend on the value of α . Fig. B1 shows that the intrinsic SED of blazars at $E > 100$ GeV in our formalism (Section 3) will be severely different than the one given by equation 13. The τ_{γ} values for our fiducial EBL model are available online.⁵

APPENDIX C: FRACTION OF TYPE-2 QSOS

In Section 3, the full SED of QSOs (k_{ν}) has been constructed to reproduce the X-ray and γ -ray background measurements. For such a constructed SED, the frequency dependent ratio of Type-2 QSO SED and full SED, $k_{\nu}^{\text{Q2}}/k_{\nu}$, can be interpreted as the fraction of the type-2 QSOs which is luminosity weighted and redshift independent. This fraction is decided by our constructed SED of type-1 QSOs in the X-ray energies, which depends on the value of α . Note that we have also included blazar contribution in k_{ν}^{Q2} . In the left-hand panel of Fig. C1 we plot the ratio $k_{\nu}^{\text{Q2}}/k_{\nu}$ for different values of α (from equation 11 to 13). The α dependence can be easily seen in the plot. The small value of α leads to less emissivity from type-1 QSOs re-

Table A1. Escape fraction measurements.

(1) Reference	(2) z -range	(3) z_{mean}	(4) λ_i (Å)	(5) $\left(\frac{f_{\lambda_{\text{FUV}}}}{f_{\lambda_i}}\right)$	(6) $f_{\text{esc}}^{\text{rel}} (1-\sigma)$	(7) $\left(\frac{f_{\lambda_{\text{FUV}}}}{f_{\lambda_i}}\right)_{\text{KS15}}$	(8) $10^{0.4A_{\text{FUV}}}$	(9) $f_{\text{esc}} (1-\sigma)$
Rutkowski et al. (2016)	0.90 – 1.40	1.15	900	7.0	< 0.027	5.63	6.07	< 0.0036
Siana et al. (2010)	1.20 – 1.50	1.35	700	3.0	< 0.006	8.40	5.91	< 0.0028
Rutkowski et al. (2017)	2.38 – 2.90	2.56	900	3.0	< 0.07	5.26	3.88	< 0.0316
Micheva et al. (2017) ^a	3.06 – 3.13	3.1	900	4.25	< 0.228	5.06	3.2	< 0.0849
Micheva et al. (2017) ^b	3.06 – 3.13	3.1	900	4.25	< 0.06	5.06	3.2	< 0.0223
Grazian et al. (2017) ^c	3.27 – 3.40	3.3	900	3.0	< 0.103	5.0	3.0	< 0.0572
Guaita et al. (2016)	3.11 – 3.53	3.4	900	5.0	< 0.12	5.18	2.91	< 0.0427
Japelj et al. (2017) ^d	3.0 – 4.0	3.5	900	3.0	< 0.20	4.96	2.83	< 0.1168
Marchi et al. (2017)	3.5 – 4.5	3.81	895	3.0	0.09 ± 0.04	5.6	2.6	0.065 ± 0.029
Matthee et al. (2017) ^e	2.20 – 2.24	2.22	H α					< 0.028

Notes: Corresponding to the references provided in column(1), the column(2) and (3) provides range in redshifts and the mean redshift for the observed sample of galaxies, column (4) provides rest frame extreme-UV wavelength λ_i where Lyman-continuum has been observed, column (5) gives the fiducial values of $f_{\lambda_{\text{FUV}}}/f_{\lambda_i}$ and column (6) gives the $1-\sigma$ values of relative escape fraction $f_{\text{esc}}^{\text{rel}}$ obtained in these references. Column (6) and (7) provides fiducial values of $f_{\lambda_{\text{FUV}}}/f_{\lambda_i}$ denoted as $(f_{\lambda_{\text{FUV}}}/f_{\lambda_i})_{\text{KS15}}$ and the dust corrections ($10^{0.4A_{\text{FUV}}}$) used in our galaxy emissivity model. Column (7) provides the absolute escape fraction values relevant to our galaxy model obtained by using equation A1. These are plotted in the left-hand panel of Fig. 3.

^a Observed for a sample of Lyman- α emitters.

^b Observed for a sample of Lyman-break galaxies.

^c Obtained for the galaxies with luminosity $> 0.2 L^*$.

^d Obtained for the galaxies with luminosity $> 0.5 L^*$.

^e The measurement is obtained using the H α emission from galaxies.

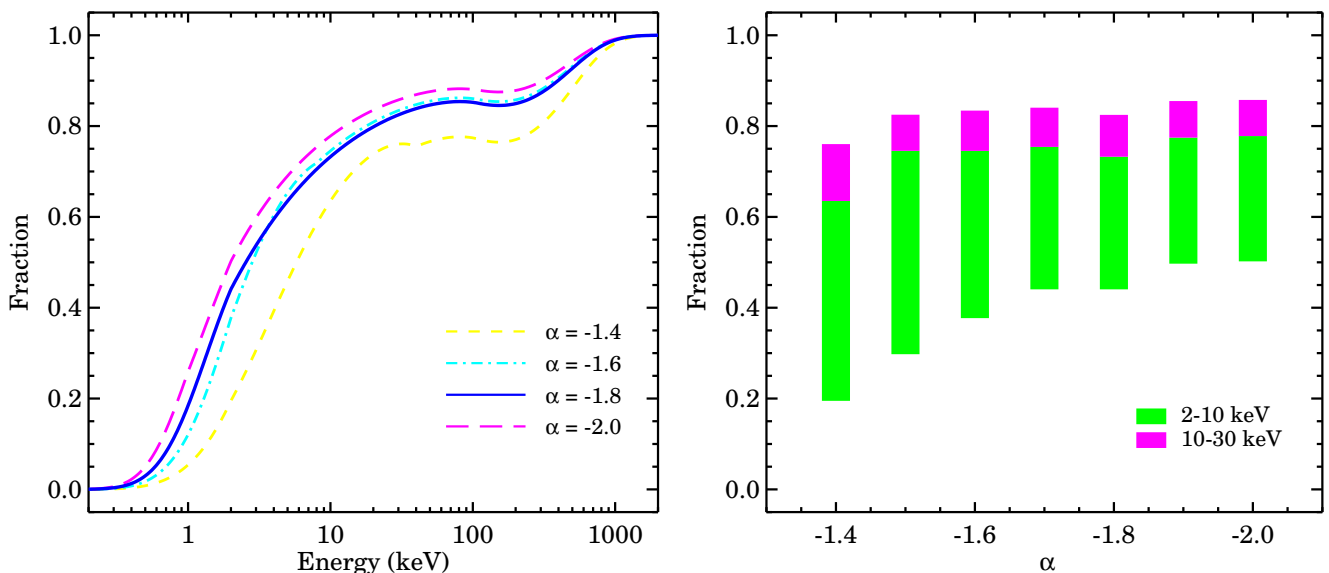


Figure C1. *Left-hand panel:* The fraction of type-2 QSOs defined as a ratio $k_{\nu}^{\text{Q2}}/k_{\nu}$ (see Section 3, equation 11 to 13) with energy in keV. The fraction also gives contribution of type-2 QSOs and blazars to EBL relative to type-1 QSOs for the SED templates used in our model. It depends on the extreme-UV power-law index α of the type-1 QSO SED. At very high energies, fraction reaches unity due to blazar contribution included in the k_{ν}^{Q2} . *Right-hand panel:* The range in the fraction of type-2 QSOs in two energy ranges, 2–10 keV and 10–30 keV, for different values of α . The fraction in the energy range 2–10 keV and 10–30 keV can be thought as the fraction of type-2 QSOs that are Compton thin and Compton thick, respectively. Out of total type-2 QSOs, 20–30% contribution comes from Compton thick QSOs.

quiring more contribution from type-2 QSOs giving rise to the higher value of their fraction. At energies less than 1 keV (2 keV), the fraction of type-2 QSOs is less than 0.2 (0.5) for all α . At energies less than 500 eV, the contribution from type-2 QSOs drops below 5%. Type-2 QSOs contribute significantly at hard X-ray energies around 10-100 keV consistent with the requirement of large number of highly obscured type-2 QSOs in X-ray population synthesis models. At energies more than 1000 keV, the fraction of type-2 QSOs is unity owing to the fact that blazars are sole contributors at these energies (see also Draper & Ballantyne 2009). For comparison with the definition of the Compton thin and Compton thick type-2 QSOs, as the contribution to X-ray background at energies 2-10 keV and 10-30 keV respectively, we plot a range in the fraction at these energies for different values of α in the right-hand panel of the Fig. C1. We find that the fraction of Compton thin QSOs to vary between 0.2-0.8 for different α . It is 0.44-0.73 for our fiducial $\alpha = -1.8$ model. For $\alpha \leq -1.5$, it varies from 0.38 to 0.78. These values are consistent with recent measurements (for e.g., Buchner et al. 2015; Georgakakis et al. 2017; Vito et al. 2017) as well as with the prediction from X-ray population synthesis models (Treister & Urry 2006; Gilli et al. 2007). We need 20-30% more contribution in 10-30 keV energy range from Compton thick QSOs, consistent with the predictions from Draper & Ballantyne (2009), however, it depends on the contribution of blazars which we do not resolve. All this interpretation is subject to our construction of type-1 QSO SED in X-rays. One can always adjust it to get different numbers while being consistent with the observed X-ray and γ -ray background. Note that, our motivation is not to understand the fraction of type-2 QSOs but to provide an observationally consistent high-energy background.

APPENDIX D: EBL MODELS WITH DIFFERENT VALUES OF α

Here, we provide the EBL models (plots and tables) obtained for different values of α ranging from -1.4 (Shull et al. 2012; Stevans et al. 2014) to -2.0 (Lusso et al. 2013; Khaire 2017) in the interval of 0.1. Fig. D1 shows photoionization rates $\Gamma_{\text{H}\,\text{I}}(z)$ and $\Gamma_{\text{He}\,\text{II}}(z)$, Fig. D2 shows photoheating rates $\xi_{\text{H}\,\text{I}}$ and $\xi_{\text{He}\,\text{II}}$ and Tables D1 to D7 provide these values for EBL models with different α from $z=0$ to 15 including for He I. Fig. D3 shows the local EBL from FIR to γ -rays and Fig. D4 shows UVB at redshifts $z = 0$ to 5. Refer to Section 4 for the relevant discussion on the trends seen in these plots.

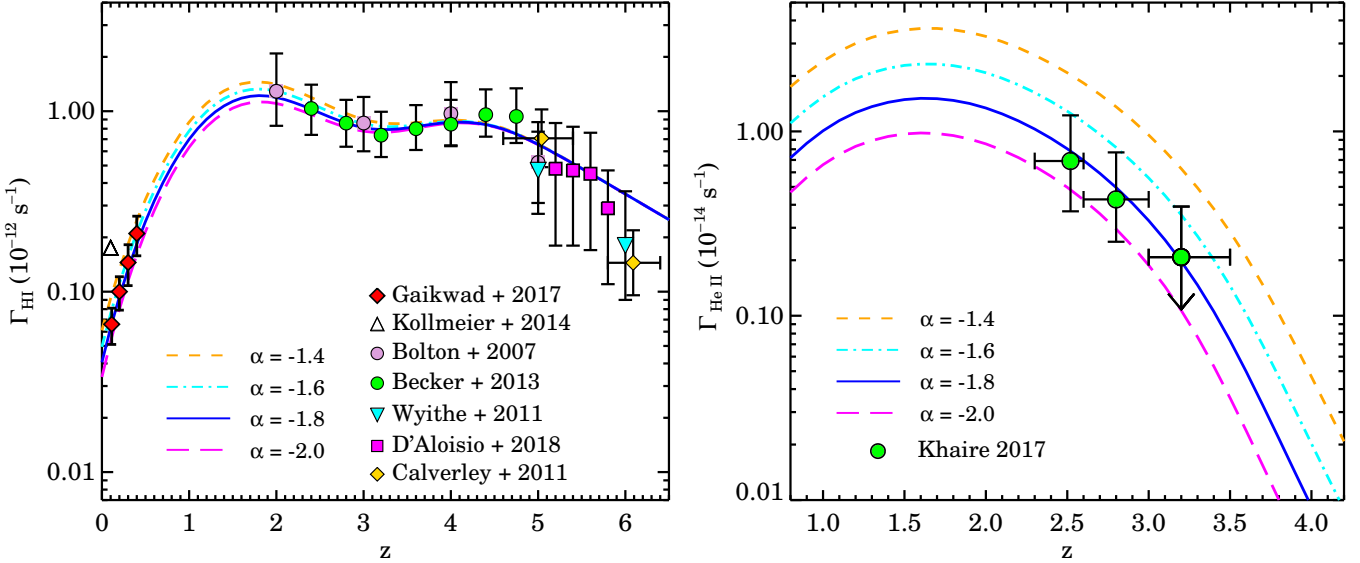


Figure D1. The photoionization rates of H I (Γ_{HI} ; left-hand panel) and He II (Γ_{HeII} ; right-hand panel) with z from UVB models with different α . Various data points in the left-hand panel show the recent measurements of Γ_{HI} . The Γ_{HeII} from Khaire (2017) is obtained by using the measurements of $\tau_{\alpha}^{\text{HeII}}$ from Worseck et al. (2016).

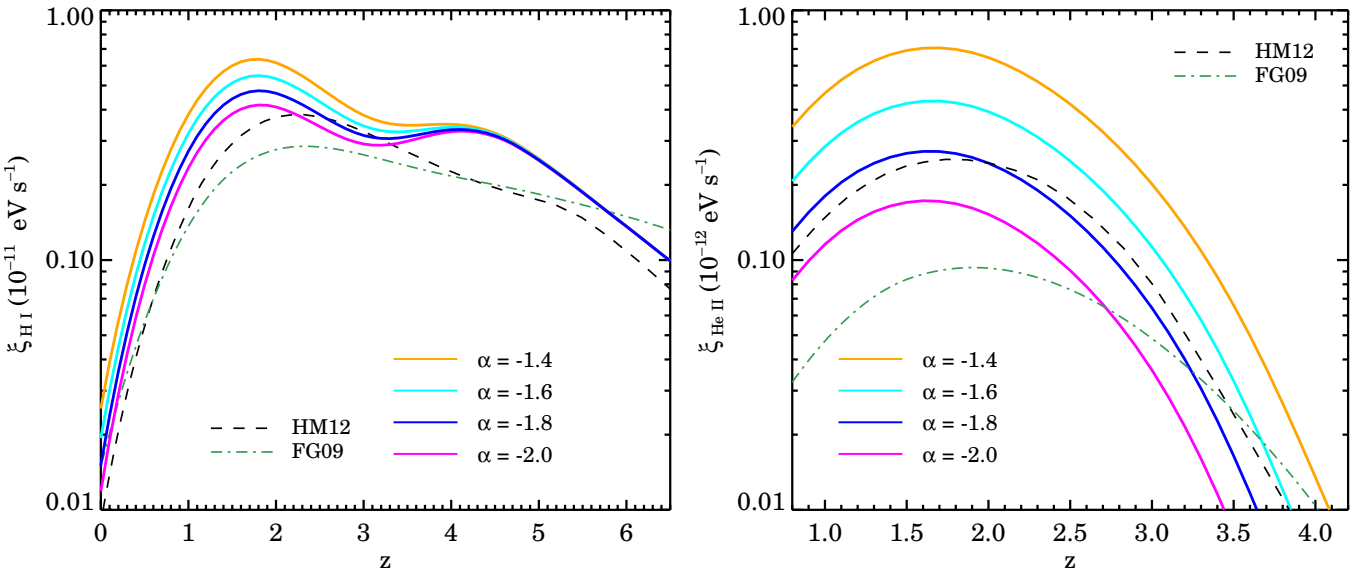


Figure D2. The photoheating rates of H I (ξ_{HI} ; left-hand panel) and He II (ξ_{HeII} ; right-hand panel) with z from UVB models with different α . The dash and dot-dash curve show the results from UVB models of HM12 and FG09, respectively.

Table D1. Photoionization and photoheating rates for our fiducial Q18 UVB model.

z	Γ_{HI} s^{-1}	Γ_{HeI} s^{-1}	Γ_{HeII} s^{-1}	ξ_{HI} eV s^{-1}	ξ_{HeI} eV s^{-1}	ξ_{HeII} eV s^{-1}
0.0	4.058e-14	1.869e-14	6.262e-16	1.507e-13	1.494e-13	1.248e-14
0.1	6.310e-14	3.041e-14	9.453e-16	2.381e-13	2.383e-13	1.857e-14
0.2	9.353e-14	4.695e-14	1.378e-15	3.575e-13	3.640e-13	2.670e-14

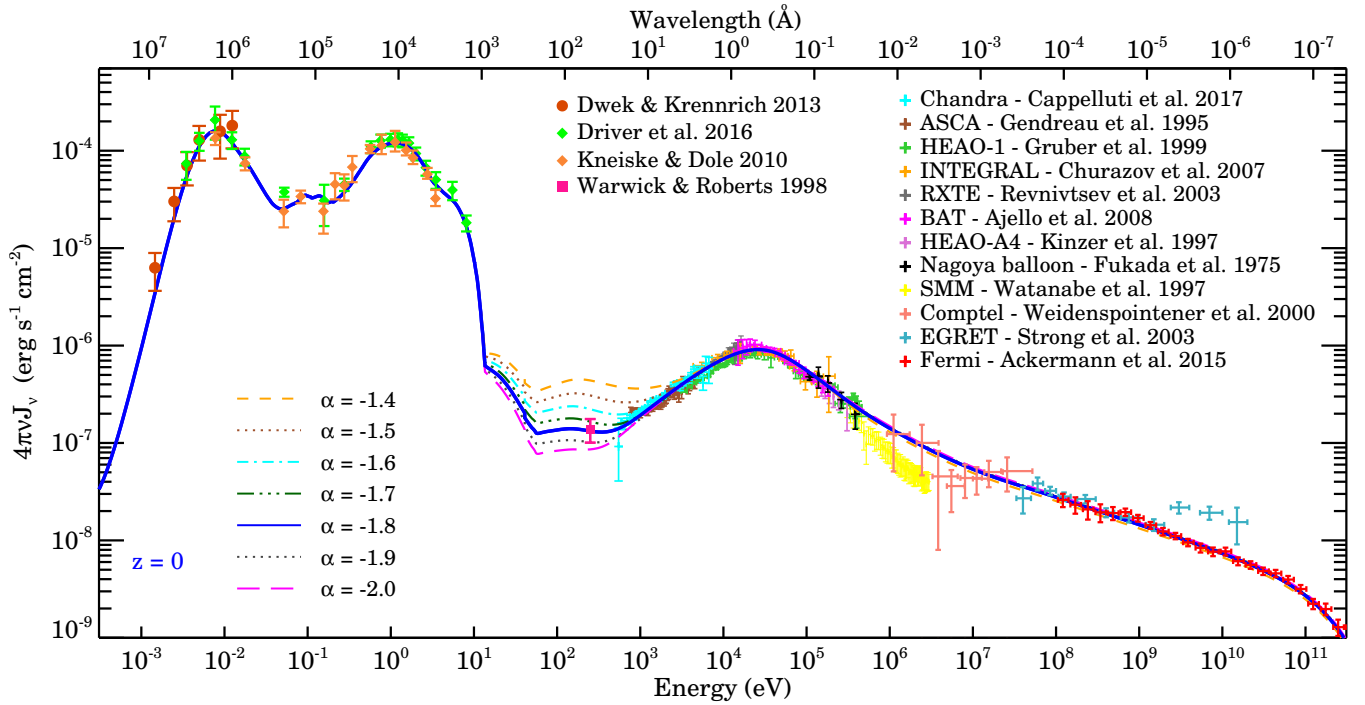


Figure D3. The intensity of $z = 0$ EBL models with different α from FIR to TeV γ -rays. For details on data points refer to Section 4.3.

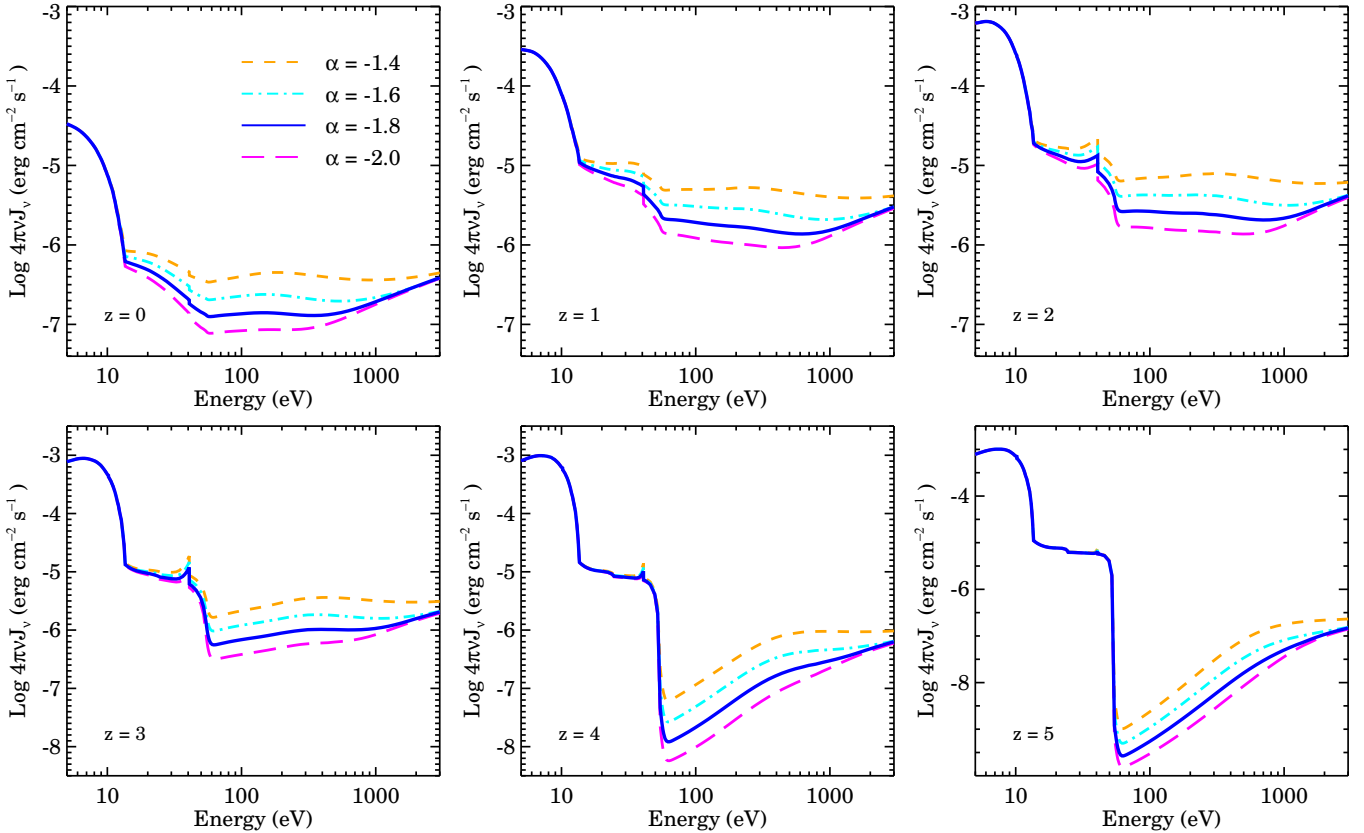


Figure D4. Spectrum of UVB models obtained for different values of α with energy (from 5 to 3000 eV) at $z = 0, 1, 2, 3, 4$ and 5. Solid blue curves show our fiducial UVB models with $\alpha = -1.8$. The y -axis scales are kept same for top three panels and bottom two panels to see relative change in intensity.

Table D2. Photoionization and photoheating rates for Q14 UVB model.

z	$\Gamma_{\text{H I}}$ s^{-1}	$\Gamma_{\text{He I}}$ s^{-1}	$\Gamma_{\text{He II}}$ s^{-1}	$\xi_{\text{H I}}$ eV s^{-1}	$\xi_{\text{He I}}$ eV s^{-1}	$\xi_{\text{He II}}$ eV s^{-1}
0.0	6.105e-14	3.709e-14	1.755e-15	2.544e-13	3.467e-13	3.675e-14
0.1	9.188e-14	5.816e-14	2.588e-15	3.895e-13	5.325e-13	5.372e-14
0.2	1.324e-13	8.706e-14	3.692e-15	5.691e-13	7.863e-13	7.588e-14

Table D3. Photoionization and photoheating rates for Q15 UVB model.

z	$\Gamma_{\text{H I}}$ s^{-1}	$\Gamma_{\text{He I}}$ s^{-1}	$\Gamma_{\text{He II}}$ s^{-1}	$\xi_{\text{H I}}$ eV s^{-1}	$\xi_{\text{He I}}$ eV s^{-1}	$\xi_{\text{He II}}$ eV s^{-1}
0.0	5.480e-14	3.099e-14	1.339e-15	2.214e-13	2.773e-13	2.745e-14
0.1	8.320e-14	4.907e-14	1.989e-15	3.418e-13	4.304e-13	4.039e-14
0.2	1.208e-13	7.403e-14	2.856e-15	5.031e-13	6.412e-13	5.741e-14

Table D4. Photoionization and photoheating rates for Q16 UVB model.

z	$\Gamma_{\text{H I}}$ s^{-1}	$\Gamma_{\text{He I}}$ s^{-1}	$\Gamma_{\text{He II}}$ s^{-1}	$\xi_{\text{H I}}$ eV s^{-1}	$\xi_{\text{He I}}$ eV s^{-1}	$\xi_{\text{He II}}$ eV s^{-1}
0.0	4.944e-14	2.602e-14	1.027e-15	1.938e-13	2.234e-13	2.071e-14
0.1	7.568e-14	4.162e-14	1.536e-15	3.016e-13	3.502e-13	3.064e-14
0.2	1.107e-13	6.333e-14	2.220e-15	4.472e-13	5.266e-13	4.379e-14

Table D5. Photoionization and photoheating rates for Q17 UVB model.

z	$\Gamma_{\text{H I}}$ s^{-1}	$\Gamma_{\text{He I}}$ s^{-1}	$\Gamma_{\text{He II}}$ s^{-1}	$\xi_{\text{H I}}$ eV s^{-1}	$\xi_{\text{He I}}$ eV s^{-1}	$\xi_{\text{He II}}$ eV s^{-1}
0.0	4.468e-14	2.194e-14	7.955e-16	1.701e-13	1.814e-13	1.586e-14
0.1	6.895e-14	3.540e-14	1.196e-15	2.670e-13	2.870e-13	2.357e-14
0.2	1.015e-13	5.425e-14	1.738e-15	3.984e-13	4.350e-13	3.382e-14

Table D6. Photoionization and photoheating rates for Q19 UVB model.

z	$\Gamma_{\text{H I}}$ s^{-1}	$\Gamma_{\text{He I}}$ s^{-1}	$\Gamma_{\text{He II}}$ s^{-1}	$\xi_{\text{H I}}$ eV s^{-1}	$\xi_{\text{He I}}$ eV s^{-1}	$\xi_{\text{He II}}$ eV s^{-1}
0.0	3.685e-14	1.586e-14	4.860e-16	1.332e-13	1.221e-13	9.640e-15
0.1	5.775e-14	2.604e-14	7.368e-16	2.121e-13	1.967e-13	1.439e-14
0.2	8.619e-14	4.048e-14	1.079e-15	3.205e-13	3.029e-13	2.075e-14

Table D7. Photoionization and photoheating rates for Q20 UVB model.

z	$\Gamma_{\text{H I}}$ s^{-1}	$\Gamma_{\text{He I}}$ s^{-1}	$\Gamma_{\text{He II}}$ s^{-1}	$\xi_{\text{H I}}$ eV s^{-1}	$\xi_{\text{He I}}$ eV s^{-1}	$\xi_{\text{He II}}$ eV s^{-1}
0.0	3.364e-14	1.361e-14	3.860e-16	1.187e-13	1.015e-13	7.721e-15
0.1	5.309e-14	2.250e-14	5.867e-16	1.903e-13	1.649e-13	1.152e-14
0.2	7.974e-14	3.519e-14	8.619e-16	2.893e-13	2.555e-13	1.662e-14

Full Tables D1 - D7 in machine-readable format are available to download at [IUCRAA-ftp](#) and a [webpage](#).